

# Shear-thinning mediation of elasto-inertial Taylor-Couette flow

Tom Lacassagne<sup>1,3†</sup>, Neil Cagney<sup>2</sup>, and Stavroula Balabani<sup>1‡</sup>

<sup>1</sup>Flume, Department of Mechanical Engineering, University College London (UCL), London, WC1E 7JE, UK

<sup>2</sup>School of Engineering and Materials Science, Queen Mary University of London, UK

<sup>3</sup>IMT Lille Douai, CERI Energie Environnement, Université de Lille, F-59000, Lille, France

(Received xx; revised xx; accepted xx)

We study the shear-thinning mediation of elasto-inertial transitions in Taylor-Couette flow of viscoelastic polymer solutions. Two types of high molecular weight polymers are used at various concentrations and in water-glycerol solvents of various viscosities. This allows us to access a wide range of elastic numbers and effective shear-thinning indices. Conservative ramp up (slow acceleration of the inner cylinder and subsequent increase in Reynolds number) and steady state (constant rotation speed) experiments are performed, in which the flow is monitored continuously using flow visualisation. Depending on the shear-thinning and elastic properties of the working fluid, very different behaviours are observed. In almost constant-viscosity fluids (Boger fluids), or shear-thinning fluids with significant elasticity, the flow transitions from purely azimuthal Couette flow (CF) to a highly chaotic flow state referred to as elasto-inertial turbulence (EIT) via Taylor Vortex Flow (TVF) and elasto-inertial waves (RSW). When the degree of shear-thinning is increased and elasticity reduced, elastic waves or EIT may fade to a Wavy Taylor Vortex Flow (WTVF) with increasing inertia. Significant shear-thinning leads to a delay in the onset of EIT. Remarkably, in some highly shear-thinning cases, even with a significant elasticity, elastic flow features (EIT, RSW) are completely suppressed, and the flow exhibit a “Newtonian-like” transition sequence (CF-TVF-WTVF). Shear-thinning acts to modify, delay, or even completely suppress elasto-inertial behaviours (RSW, EIT), that would otherwise have existed in the absence of shear-thinning. It is, thus, possible to induce various hydrodynamic regimes by tuning the relative degrees of shear-thinning, elasticity, and inertia.

**Key words:** Viscoelasticity, Shear-thinning, Taylor-Couette

## 1. Introduction and background

Taylor-Couette flow (TCF) occurs in the gap between two concentric cylinders with one or both rotating. It has been of sustained interest to the fluid mechanics community, rheologists, process engineers and mathematicians over the past century (Taylor 1923). Despite its simple geometrical configuration, Taylor-Couette flow of Newtonian fluids displays a vast array of complex dynamics. This includes a wide variety of steady, unsteady, chaotic or turbulent flow states (Andereck *et al.* 1986; Coles 1965; Dutcher &

† Email address for correspondence: tom.lacassagne@imt-lille-douai.fr

‡ Email address for correspondence: s.balabani@ucl.ac.uk

38 Muller 2009; Akonur & Lueptow 2003; Grossmann *et al.* 2016; Gul *et al.* 2018), occurring  
 39 when either one or two cylinders rotate, in contra- or co-rotation. In the most common  
 40 case in which only the inner cylinder rotates and the outer cylinder is fixed, the flow can  
 41 be characterised using a single Reynolds number:

$$\text{Re} = \rho\Omega r_i d / \mu, \quad (1.1)$$

42 where  $\rho$  is the fluid density,  $\mu$  the dynamic viscosity,  $\Omega$  the inner cylinder rotation speed  
 43 and  $d = r_o - r_i$  the gap width, i.e. the difference between the inner and outer cylinder  
 44 radii,  $r_i$  and  $r_o$  respectively. The system geometry can be characterised using two non-  
 45 dimensional parameters: the radius ratio  $\eta = r_i / r_o$  and the aspect ratio  $\text{AR} = L / d$  where  
 46  $L$  is the cylinder length. The first parameter describes the gap width and streamline  
 47 curvature in a simple shear flow, both having an influence on the stability threshold for  
 48 Newtonian (Taylor 1923) but also non-Newtonian fluids (Larson *et al.* 1990; Pakdel &  
 49 McKinley 1996).

50 At low  $\text{Re}$  in Newtonian fluids, a purely azimuthal and uniform shear flow exists in the  
 51 gap, known as the circular Couette flow (CF). This flow becomes unstable once a critical  
 52  $\text{Re}$  is reached, and a series of toroidal counter-rotating vortices form in the annulus: this  
 53 is known as the Taylor vortex flow (TVF). The number of counter rotating vortices along  
 54 the gap corresponds to the spatial wavelength of the instability,  $\lambda$ . A further increase in  
 55  $\text{Re}$  causes this state to become unstable and undergo sinusoidal axial oscillations (Wavy  
 56 Taylor Vortex Flow, WTVF), making it non-axisymmetric. Additional frequencies appear  
 57 as  $\text{Re}$  is further increased, leading to a more complex wavy flow (Coughlin & Marcus  
 58 1992*a,b*) which ultimately becomes turbulent (Grossmann *et al.* 2016).

59 Because of this rich set of dynamic states in simple fluids, Taylor-Couette flow has  
 60 been widely used as a means to study flow transitions and instabilities in more complex  
 61 systems, such as non-Newtonian fluids (Fardin *et al.* 2014), frequently encountered in  
 62 industrial applications (Chhabra & Richardson 1999). Polymer solutions (Larson & Desai  
 63 2015) or Wormlike Micellar Solutions (WMS) (Divoux *et al.* 2016) are useful model fluids  
 64 to describe the behaviour of such systems. The latter have received increased attention  
 65 in recent years (Fardin *et al.* 2010, 2012; Perge *et al.* 2014; Mohammadigoushki & Muller  
 66 2017; Hopkins *et al.* 2020; Haward *et al.* 2020) while the former have been extensively  
 67 used in the literature for several decades (see remainder of section 1), and will also be  
 68 employed in this study. Two of their most common non-Newtonian properties are shear-  
 69 thinning and viscoelasticity. The former leads to a dynamic viscosity  $\mu$  that depends  
 70 on the shear rate  $\dot{\gamma}$  (e.g. in a power law fashion,  $\mu \sim \dot{\gamma}^{n-1}$  with  $n$  the flow index).  
 71 Elasticity confers a “solid-like” behaviour to the fluid, with a complex shear modulus  
 72  $G^*$  that comprises an elastic part  $G'$  and a viscous part  $G''$  such as  $G^* = G' + iG''$ .  
 73 This property is characterized by the existence of an elastic/relaxation time-scale of the  
 74 fluid,  $t_e$ . Such properties are influenced by many factors including the molecular weight,  
 75 polymer concentration, conformation of the polymer chains, and entanglement (Larson  
 76 & Desai 2015). By using low concentrations of high molecular weight linear polymers in  
 77 a sufficiently viscous solvent, one may produce “Boger” fluids (Boger 1977; James 2009),  
 78 i.e. elastic fluids for which the polymer contribution to the viscosity is small compared to  
 79 the solvent viscosity, and for which the apparent viscosity is thus constant (Newtonian).  
 80 Equally, by selecting different polymers and solvent viscosities, one can vary elasticity and  
 81 shear-thinning almost independently, exploring the relative influence of these parameters  
 82 on TCF over a broad parameter space.

### 1.1. Elastic and elasto-inertial Taylor-Couette flows

The degree to which a fluid has an elastic response to the flow is expressed by the Weissenberg number,  $Wi$ . In a Taylor-Couette system, this number can be defined as  $Wi = t_e/\dot{\gamma}$ , where  $\dot{\gamma} = \Omega r_i/d$  is the nominal shear-rate in the gap. The competition between elastic and viscous effects is then expressed by the elastic number:

$$El = \frac{Wi}{Re} = \frac{t_e}{t_v} = \frac{t_e\mu}{\rho d^2}, \quad (1.2)$$

where  $t_v = \rho d^2/\mu$  is the viscous time-scale.  $El$  only depends on the fluid and geometric properties. Based on its value, the fluid can be classified as weakly elastic ( $El < 10^{-2}$ ), moderately elastic ( $10^{-2} < El < 1$ ), or highly elastic ( $El > 1$ ) (Latrache *et al.* 2016; Dutcher & Muller 2011, 2013). In the range of low elasticity (i.e.,  $El \ll 1$ ) and with increasing  $Re$ , transitions similar to Newtonian fluids have been recovered (Crumeyrole *et al.* 2002; Dutcher & Muller 2011).

At vanishing  $Re$  but moderate or high  $El$ , a purely elastic CF-TVF transition exists (Larson *et al.* 1990), and flows may even exhibit a chaotic behaviour (Groisman & Steinberg 2004; Fardin *et al.* 2010, 2012; Mohammadigoushki & Muller 2017), which is called elastic “turbulence”, despite the relative absence of inertia (Larson 2000), as it shows chaotic and disordered features usually attributed to turbulence (Groisman & Steinberg 2000; Varshney & Steinberg 2019; Steinberg 2019).

At both non-negligible  $Re$  and  $El$  values, elasto-inertial instabilities (primary or secondary) occur (Steinberg & Groisman 1998). They involve non-axisymmetric flow states and standing or travelling elastic waves such as ribbons (RIB) (Baumert & Muller 1999; Latrache *et al.* 2016), spiral vortex flow (SVF) (Avgousti & Beris 1993; Mohammadigoushki & Muller 2017) and rotating spiral waves (RSW) (Groisman & Steinberg 1996; Thomas *et al.* 2006; Dutcher & Muller 2013; Lacassagne *et al.* 2020). Upon increasing  $Re$  or  $El$ , such pre-chaotic states are replaced by unsteady, chaotic flow states, that have been called disordered oscillations (DO) (Groisman & Steinberg 1996), defect mediated turbulence (DMT) or spatio-temporal intermittency (STI) (Latrache *et al.* 2012, 2016). They all consist in a gradual transition to elasto-inertial turbulence (EIT) (Dutcher & Muller 2013; Liu & Khomami 2013; Perge *et al.* 2014; Lacassagne *et al.* 2020). Elasto-inertial (and elastic) turbulence induces spatial and temporal chaos in fluids that would otherwise have been flowing in laminar states without elasticity, promoting mixing and momentum transfer (Groisman & Steinberg 2004).

### 1.2. Shear-thinning Taylor-Couette flows with negligible elasticity

In shear-thinning fluids with negligible elasticity, the typical transition pattern is “Newtonian-like”: CF-TVF-WTVF (Escudier *et al.* 1995; Bahrani *et al.* 2015; Topayev *et al.* 2019; Cagney & Balabani 2019*b*). In the small gap limit, a decrease in the critical Reynolds number for the formation of Taylor vortices  $Re_c^{TVF}$  (destabilisation) occurs with increased shear-thinning. This has been observed both experimentally (Cagney *et al.* 2020; Cagney & Balabani 2019*a*; Escudier *et al.* 1995) and numerically (Ashrafi & Khayat 2000; Caton 2006). In the large gap limit, shear-thinning has a non-monotonic effect on  $Re_c^{TVF}$ , (Sinevic *et al.* 1986; Lockett *et al.* 1992; Cagney & Balabani 2019*a*; Alibenyahia *et al.* 2012).

The spatial wavelength of the TVF has been found to increase with increased shear-thinning, as observed in experiments and the linear stability analysis by Bahrani *et al.* (2015) (in a large gap flow cell), laser-Doppler velocimetry measurements by Escudier *et al.* (1995), or particle image velocimetry (PIV) in Cagney & Balabani (2019*b*). From

the two later works and recent numerical simulations by Topayev *et al.* (2019) and Alibenyahia *et al.* (2012), shear-thinning was found to modify the structure of the Taylor vortices, by making individual vortices asymmetric, and increasing the amplitudes of the travelling waves at the inward and outward jets. Sparse data on the critical Re value for the TVF to WTVF (Bahrani *et al.* 2015; Cagney *et al.* 2020) suggest that the TVF to WTVF transition happens at lower Re values with increased shear-thinning. Shear-thinning also alters the structure of the wavy vortices (Cagney & Balabani 2019*b*; Cagney *et al.* 2020).

### 1.3. Combined shear-thinning and elasticity

The effects of shear-thinning and elasticity have been studied separately in the literature, with elastic fluids having received more attention to date. There is still a lack of experimental work on fluids combining the two properties. In studies focused on elastic fluids, shear-thinning, when reported, is generally mild and typically neglected. However, even moderate shear-thinning can have a significant impact on the base flow structure, and thus on the development of elastic instabilities. The onset of the primary instability is found at lower critical Re values than in Newtonian fluids, regardless of shear-thinning (Larson *et al.* 1994; Crumeyrolle *et al.* 2002; Dutcher & Muller 2011, 2013; Schaefer *et al.* 2018; Cagney & Balabani 2019*b*; Cagney *et al.* 2020). The main challenge resides in describing higher order, higher Re flow transitions.

Latrache and co-workers performed a series of experimental works using shear-thinning and viscoelastic PolyEthylene Oxide (PEO) solutions in low viscosity solvents. They reported several types of transition patterns, from Newtonian-like (Crumeyrolle *et al.* 2002) at  $El < 0.03$ , to “elastic-like” with RIB (Crumeyrolle *et al.* 2002, 2005) and EIT states (Latrache *et al.* 2012, 2016; Abcha *et al.* 2018). In Crumeyrolle *et al.* (2005) and Latrache *et al.* (2016), defect mediated turbulence was reported, entailing a local collision of RIB waves leading to a spatio-temporal heterogeneity of the RIB map. The multiplication of such features ultimately leads to a fully disordered flow that can be labelled DO or EIT. In a recent work (Lacassagne *et al.* 2020), we reported an analog behaviour of elasticity promoting local anomalies in the flow, this time in a non-shear-thinning Boger fluid. The mechanism was yet different from DMT, as it consisted in merging and splitting of base Taylor vortices crossed by axial RSW waves, instead of defects in RIB amplitude. It thus appears that the mechanisms for transition to EIT are greatly affected by the shear-thinning behaviour of the fluid.

Dutcher & Muller (2009, 2011, 2013) also used shear-thinning and elastic PEO solutions, to study the effects of weak and intermediate elasticity. Comparing their results with those of Crumeyrolle *et al.* (2002), the authors argued that the difference in the ratio of polymer and solvent viscosity may explain the different flow transitions observed at similar El values. This polymer-to-solvent viscosity ratio is intrinsically related to the shear-thinning property: the higher this ratio, the more the polymer contributes to the overall viscosity and the stronger the shear-thinning level is likely to become.

In our recent work (Cagney *et al.* 2020), xanthan gum (XG) solutions with systematically increasing concentration were produced, yielding fluids with both increasing shear-thinning and elastic properties. Even at high El values, the Newtonian-like transition pattern associated with shear-thinning fluids was retrieved, and no typical features of elastic behaviours (RSW, RIB, EIT) were reported. In this study, as in those of Latrache and co-workers, disentangling the effects of shear-thinning and elasticity was difficult, as both properties were varied simultaneously with the polymer concentration. Moreover, many previous studies examining TC flow of XG solutions did not fully characterise the rheology and assumed negligible elasticity, making it challenging to distinguish the effects

177 of either phenomenon on the flow (Elçiçek & Güzel 2020*a,b*; Bahrani *et al.* 2015; Masuda  
178 *et al.* 2017).

179 Finally, in TC flows of shear-thinning and elastic WMS, travelling vortices (SVF),  
180 standing waves (RIB) and transition to EIT have been reported. In Perge *et al.* (2014) the  
181 typical transition pattern is CF-RIB-EIT in a significantly shear-thinning fluid ( $n = 0.45$ )  
182 at  $El \sim 1$ . In Mohammadigoushki & Muller (2017), travelling vortices that could be SVF  
183 were reported, as well as a transition to EIT.

184 Experimental data on Taylor-Couette flow of fluids that are both shear-thinning and  
185 viscoelastic is inconclusive regarding how shear-thinning affects elastic instabilities and  
186 transitions. It appears that elastic fluids may exhibit a Newtonian-like transition pattern,  
187 in the low elasticity limit (Dutcher & Muller 2011; Crumeyrolle *et al.* 2002), but also  
188 at high  $El$  when they are also shear-thinning (Cagney *et al.* 2020), suggesting that  
189 shear-thinning may act to reduce or suppress elastic instabilities. Such a shear-thinning  
190 modification of elastic effects has also been observed in other types of flows (PEO in  
191 serpentine micro-channel, Casanellas *et al.* (2016), WMS flow past micro-pins, Haward  
192 *et al.* (2020)). On the other hand, shear-thinning is known to be conditional for some  
193 elastic instabilities to develop, for example in viscoelastic (pressure driven) channel flows  
194 (Bodiguel *et al.* 2015; Barlow *et al.* 2019).

195 In this work, we thus aim at disentangling the effects of shear-thinning and elasticity  
196 on TCF transitions and patterns in polymer solutions. We present flow visualisation  
197 measurements of TCF for polymer solutions with variable degrees of elasticity and shear-  
198 thinning. The remainder of the paper is structured as follows. Firstly, the experimental  
199 system is described in section 2. The results of flow visualisation experiments are then  
200 reported in section 3. In section 4, the combined effects of shear-thinning and elasticity  
201 on transitions to TVF and WTVF and EIT, including potential suppression of the latter,  
202 are discussed, and some concluding remarks can be found in section 5.

## 203 2. Experiments

204

### 2.1. Taylor-Couette cell

205 The experiments were performed in a custom made Taylor-Couette flow cell. It com-  
206 prised an outer cylinder made of an acrylic pipe, mounted vertically between two acrylic  
207 plates, and a black PTFE inner cylinder. The latter had a conical tip complementary to  
208 a dent in a bottom plate which allowed to reduce bottom friction while, together with  
209 a ball bearing at the top lid, ensuring alignment between inner and outer cylinder. The  
210 top and bottom lids were stationary, with a  $\sim 3$  mm gap between lid and cylinder at  
211 both ends. The cylinder was driven from the top using a stepper motor (SmartDrive Ltd,  
212 Cambridge, U.K.), the rotation of which could be controlled to a high degree of precision  
213 by a 52 000 microstep/revolution controller (SmartDrive Ltd, Cambridge, U.K.). The  
214 inner chamber, which was completely filled with working fluid, had an axial length of  
215  $L = 135$  mm. The inner and outer radii of the flow cell were 21.66 mm and 27.92 mm,  
216 respectively. The radius ratio was thus  $\eta = 0.77$ , the gap width was  $d = 6.26$  mm, and  
217 the aspect ratio was  $AR = 21.56$ . The geometric parameters are sketched on figure 1.

218 The flow section was enclosed in a rectangular chamber in which water was recirculated  
219 via a temperature bath to ensure that the temperature remained constant and close  
220 to  $20^\circ\text{C}$  throughout experiments. The temperature within the flow cell was measured  
221 immediately before and after each experiment, and it was found to vary by less than  
222  $0.2^\circ\text{C}$ .

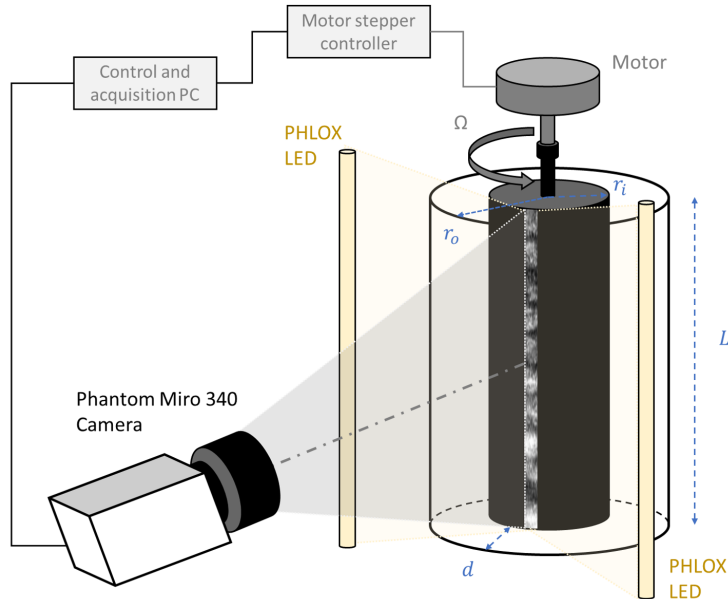


Figure 1: Sketch of the test-section and flow visualisation system.

## 2.2. Polymer solutions and rheological characterisation

Optically clear shear-thinning and viscoelastic polymer solutions were prepared by dissolving XG (Sigma Aldrich) into a mixture of glycerol and deionized water. The weight-averaged molecular mass  $M_w$  was measured by size exclusion chromatography and found equal to  $1.76 \times 10^6 \text{ g}\cdot\text{mol}^{-1}$  (Cagney *et al.* 2020).

Various degrees of elasticity and shear-thinning of the XG solutions were achieved by varying solution composition (polymer concentration and glycerol volume fractions). For comparison, a Boger fluid was prepared by dissolving small concentrations of PolyAcrylamide (PAAM,  $M_w = 5.5 \times 10^6 \text{ g}\cdot\text{mol}^{-1}$ , Sigma Aldrich) into deionized water-glycerol mixtures. Polymers were progressively added to the solvent, left to dissolve overnight without any agitation, to prevent polymer chain destruction in the preparation process, and the mixture was finally homogenised by gentle shaking. Polymer type, concentration, and solvent composition and viscosity for each working fluid used in this work are listed in table 1. The sample naming convention used throughout the paper is the following: letters correspond to the polymer used (XG for xanthan gum, P for polyacrylamide, N for none), the last two digits after the “-” sign to the glycerol volume fraction (e.g. -72 for 72%) and the middle number, if present, to the polymer concentration in ppm (parts per million in weight).

The steady-shear rheology of all working fluids was measured using a rotational rheometer (ARES, TA Instruments) equipped with a Couette geometry (inner radius 32 mm, outer radius 34 mm) in steady shear mode. All XG samples exhibit shear-thinning. The shear viscosity of PAAM sample remains almost constant for a wide range of shear rates. Flow curves (viscosity versus shear rate) for all working fluids are shown in figure 2. The shear-thinning data can be described using a Carreau model

$$\mu(\dot{\gamma}) = \mu_\infty + (\mu_0 - \mu_\infty) \left(1 + (t_c \dot{\gamma})^2\right)^{(n_c - 1)/2}, \quad (2.1)$$

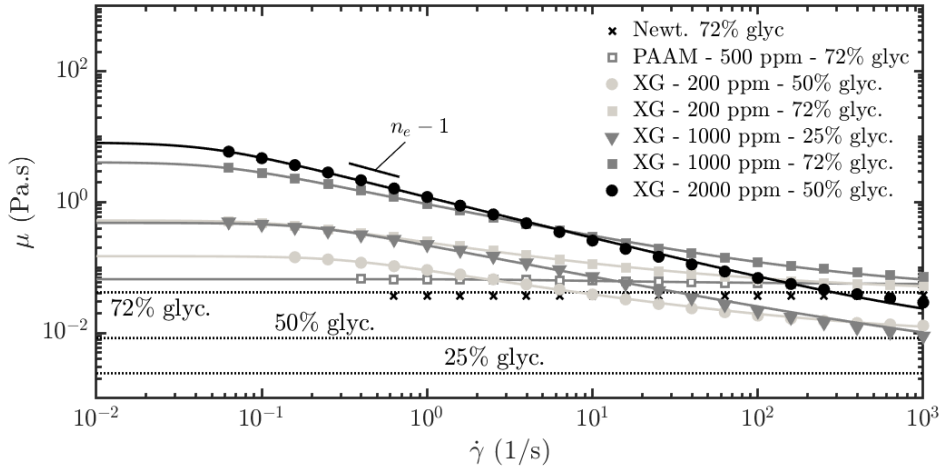


Figure 2: Viscosity as a function of shear rate for polymer solutions (filled symbols for XG, open symbols for PAAM) at various concentrations and in solvents of three different glycerol volume fractions, 25% (triangles), 50% (circles) and 72% (squares). Expected solvent constant viscosities  $\mu_s$  are derived from Volk & Kähler (2018) and plotted as dotted lines. The measured viscosity for the reference Newtonian case (72% glycerol in water) is represented by black crosses.

| ID        | Pol. | C    | Gly. | $\rho$             | $\mu_s$ | $\mu_0$ | $\mu_\infty$ | $n_c$  | $t_c$  | $\frac{\mu_0}{\mu_\infty}$ | $t_e$  |
|-----------|------|------|------|--------------------|---------|---------|--------------|--------|--------|----------------------------|--------|
|           |      | ppm  | %v   | Kg.m <sup>-3</sup> | Pa.s    | Pa.s    | Pa.s         |        | s      |                            | s      |
| N-72      | -    | 0    | 0.72 | 1198               | 0.0363  | -       | -            | -      | -      | 1.0                        | -      |
| P500-72   | PAAM | 500  | 0.72 | 1198               | 0.0363  | 0.0573  | 0.0425       | 0.6622 | 0.2268 | 1.35                       | 0.1939 |
| XG200-72  | XG   | 200  | 0.72 | 1198               | 0.0363  | 0.5027  | 0.0419       | 0.5734 | 6.949  | 12.0                       | 0.1257 |
| XG200-50  | XG   | 200  | 0.50 | 1142               | 0.0083  | 0.1291  | 0.0084       | 0.5860 | 2.895  | 15.3                       | 0.2194 |
| XG1000-72 | XG   | 1000 | 0.72 | 1198               | 0.0363  | 3.674   | 0.0419       | 0.5009 | 16.48  | 87.7                       | 11.46  |
| XG1000-25 | XG   | 1000 | 0.25 | 1072               | 0.0024  | 0.5199  | 0.0024       | 0.5386 | 6.9133 | 214                        | 2.536  |
| XG2000-50 | XG   | 2000 | 0.50 | 1142               | 0.0083  | 8.090   | 0.0084       | 0.3709 | 22.20  | 967                        | 50.24  |

Table 1: Polymer solutions and their rheological properties at 20 °C. The sample labelling scheme is the following (ID column): XXiii-jj where XX is the polymer molecule used (N if no polymer), iii is the polymer concentration in ppm (empty if no polymer), and jj is the glycerol volume fraction in the solvent in volume %.

247 where  $\mu_\infty$  and  $\mu_0$  are viscosity plateau values at infinite and zero shear respectively,  $t_c$   
248 is the characteristic Carreau time scale, and  $n_c$  is the Carreau flow index. The fitted  
249 expressions are plotted on figure 2 as full lines. The estimated parameters for each fluid  
250 are also displayed in table 1. The ratio  $\mu_0/\mu_\infty$  (reported in the last column of table 1)  
251 indicates the difference between so called Boger fluids, for which the viscosity can be  
252 assumed constant with  $\mu_0/\mu_\infty \sim 1$ , and shear-thinning fluids for which  $\mu_0/\mu_\infty \gg 1$ . For  
253 a given fluid, the degree of shear-thinning (slope of the curve) was shear-rate dependent.  
254 This means that the effective shear-thinning behaviour varied as the rotation speed was  
255 varied. It is thus convenient to define a shear rate dependent, “effective” flow index from  
256 the local slope of the flow curve in a log-log space (sketched on figure 2, see Coronado-  
257 Matutti *et al.* (2004); Cagney & Balabani (2019b); Cagney *et al.* (2020)):

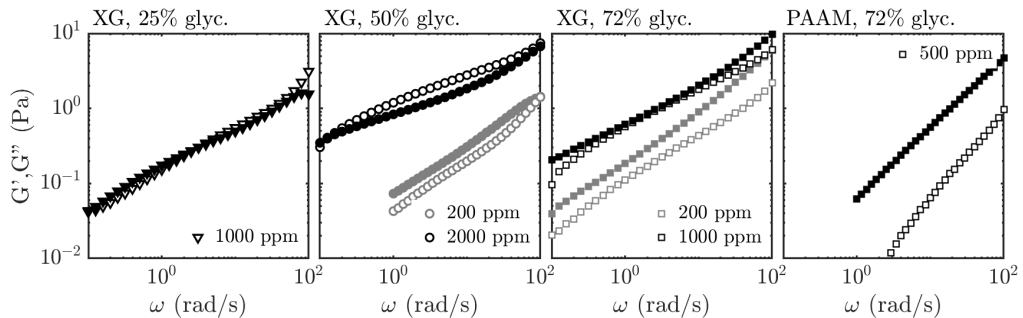


Figure 3:  $G'$  (open symbols) and  $G''$  (filled symbols) moduli for XG and PAAM solutions at various concentrations and in various glycerol water solvents.

$$n_e = \frac{\partial \log(\mu)}{\partial \log(\dot{\gamma})} + 1, \quad (2.2)$$

258 where  $n_e$  is equivalent to the previously defined flow index  $n$ , but accounts for the non-  
 259 power-law behaviour via shear-rate dependency. An effective flow index close to unity  
 260 means that the fluid behaves as a Newtonian fluid, and the effective flow index decreases  
 261 with increasing shear-thinning behaviour. While  $n_c$  may vary non-monotonically with  
 262 polymer concentration,  $n_e$  always decreases with increasing polymer concentration at  
 263 a given shear-rate and for a given solvent, and is a better indication of the degree of  
 264 shear-thinning in each fluid (Cagney *et al.* 2020).

265 The elastic properties of the samples were quantified by oscillatory shear experiments  
 266 on the same rheometer and geometry. The evolution of  $G'$  and  $G''$  with oscillation  
 267 frequency were measured for  $\gamma = 5\%$ .  $G'$  and  $G''$  frequency sweeps are shown in figure 3.

268 For this study, a common way to estimate elastic time-scales for the various types of  
 269 fluids used and compare them, regardless of the solvent contribution to viscosity, was  
 270 needed. To do so, the loss modulus curves from figure 3 were corrected by removing the  
 271 contribution of the solvent viscosity (Zirnsak *et al.* 1999), such that

$$\tilde{G}'' = G'' - \mu_s \omega. \quad (2.3)$$

272 The elastic time scale could then be obtained from the crossover frequency  $\tilde{\omega}_c$  between  
 273  $G'$  and  $\tilde{G}''$  curves (not shown on figure 3 for the sake of readability), such that  $t_e = 2\pi/\tilde{\omega}_c$ .  
 274 Doing so, one could access the polymer time-scale regardless of the solvent used (even  
 275 in fluids for which the solvent contribution to the overall viscosity is large compared to  
 276 the polymer one, and for which no crossover between  $G'$  and  $G''$  can be observed on  
 277 figure 3). Estimated time scales agreed with those estimated from Zimm approximation  
 278 or multi-mode Maxwell fitting on  $G'$  and  $G''$  curves (Öztekin *et al.* 1994).

### 2.3. Flow visualisation experiments

280 The flow was visualized by adding reflective mica flakes to the fluid (Cornelissen & Son,  
 281 Pearl Lustre Pigments), at a volume fraction of the order of  $10^{-4}$ , similar to previous  
 282 studies (Cagney & Balabani 2019b; Cagney *et al.* 2020). Images of a vertical strip along  
 283 the cylinder's axial dimension were acquired by a Phantom Miro 340 camera (see figure  
 284 1). The frame rate  $f_s$  was adjusted throughout the experiments in order to achieve high  
 285 temporal resolution of the Reynolds number range studied. For ramp up and steady



| Sample    | Test | $f_s$<br>Hz | $1/\Delta Re$ | $\Omega_{max}$<br>$s^{-1}$ | $\bar{n}_e$ | $\bar{El}$ | $d\Omega/dt$<br>$s^{-2}$ | $\Gamma_0$ | Transition sequence   |
|-----------|------|-------------|---------------|----------------------------|-------------|------------|--------------------------|------------|-----------------------|
| N72       | 1    | 75          | 224.32        | 66.96                      | 1.0         | 0          | 0.07463                  | 0.4338     | CF-TVF-WTVF           |
| N72       | 2    | 30          | 201.88        | 66.96                      | 1.0         | 0          | 0.03317                  | 0.1928     |                       |
| P500-72   | 1    | 200         | 225.56        | 99.23                      | 0.96        | 0.19       | 0.2911                   | 0.7705     | CF-TVF-RSW-EIT        |
| P500-72   | 2    | 200         | 225.56        | 99.23                      | 0.96        | 0.19       | 0.2911                   | 0.7705     |                       |
| P500-72   | 3    | 90          | 253.77        | 99.23                      | 0.96        | 0.19       | 0.1164                   | 0.3082     |                       |
| P500-72   | 4    | 90          | 255.43        | 87.64                      | 0.97        | 0.21       | 0.1023                   | 0.3473     |                       |
| P500-72   | 5    | 90          | 255.43        | 87.64                      | 0.97        | 0.21       | 0.1023                   | 0.3473     |                       |
| XG200-72  | 1    | 62          | 236.4         | 108.0                      | 0.85        | 0.88       | 0.09161                  | 0.2047     | CF-TVF-(RSW)-EIT-WTVF |
| XG200-72  | 2    | 90          | 258.4         | 107.1                      | 0.85        | 0.17       | 0.1208                   | 0.2743     |                       |
| XG200-50  | 1    | 42          | 178.9         | 36.80                      | 0.75        | 0.080      | 0.02770                  | 0.5330     | CF-TVF-RSW-WTVF       |
| XG200-50  | 2    | 42          | 178.9         | 36.80                      | 0.75        | 0.080      | 0.02770                  | 0.5330     |                       |
| XG200-50  | 3    | 62          | 281.1         | 36.18                      | 0.73        | 0.14       | 0.02549                  | 0.5078     |                       |
| XG1000-72 | 1    | 250         | 157.5         | 147.5                      | 0.72        | 35         | 0.7448                   | 0.8924     | CF-EIT                |
| XG1000-72 | 2    | 250         | 150.1         | 153.3                      | 0.71        | 13         | 0.8125                   | 0.9013     |                       |
| XG1000-72 | 3    | 50          | 157.5         | 147.5                      | 0.72        | 35         | 0.14895                  | 0.1785     |                       |
| XG1000-72 | 4    | 90          | 270.1         | 153.3                      | 0.71        | 13         | 0.1625                   | 0.1803     |                       |
| XG1000-25 | 1    | 30          | 199.9         | 46.84                      | 0.58        | 1.2        | 0.02229                  | 0.2648     | CF-TVF-WTVF           |
| XG2000-50 | 1    | 94          | 162.2         | 76.50                      | 0.46        | 67         | 0.1385                   | 0.6168     | CF-TVF-SVF-RSW-EIT    |
| XG2000-50 | 2    | 42          | 212.5         | 95.02                      | 0.56        | 74         | 0.05875                  | 0.1696     |                       |
| XG2000-50 | 3    | 200         | 235.5         | 82.75                      | 0.46        | 67         | 0.2198                   | 0.8366     |                       |
| XG2000-50 | 4    | 200         | 235.5         | 82.75                      | 0.46        | 67         | 0.2198                   | 0.8366     |                       |

Table 2: Experimental conditions for ramp up experiments, and transition sequence reported. Samples rheological characterisation is reported in table 1. CF: Couette Flow, TVF: Taylor Vortex Flow, WTVF: Wavy Taylor Vortex Flow, RSW: Rotating Spiral Waves, SVF: Spiral Vortex Flow, EIT: Elasto-Inertial Turbulence.

| Sample    | Test | $f_s$<br>Hz | $\Omega$<br>$s^{-1}$ | Re  | $\bar{n}_e$ | $\bar{El}$ | $\Gamma_0$ | State   |
|-----------|------|-------------|----------------------|-----|-------------|------------|------------|---------|
| XG200-50  | S1   | 620         | 12.22                | 76  | 0.73        | 0.14       | 0.5078     | RSW     |
| XG200-50  | S2   | 620         | 16.80                | 114 | 0.73        | 0.14       | 0.5078     | WTVF    |
| XG200-50  | S3   | 620         | 25.96                | 198 | 0.73        | 0.14       | 0.5078     | WTVF    |
| XG2000-50 | S1   | 600         | 26.44                | 52  | 0.47        | 72         | 0.2216     | SVF     |
| XG2000-50 | S2   | 600         | 31.73                | 69  | 0.47        | 72         | 0.2216     | RSW     |
| XG2000-50 | S3   | 600         | 34.37                | 79  | 0.47        | 72         | 0.2216     | RSW-EIT |
| XG2000-50 | S4   | 600         | 52.88                | 152 | 0.47        | 72         | 0.2216     | EIT     |

Table 3: Experimental conditions: Steady state experiments.  $\Gamma_0$  specifies the maximum non-dimensional acceleration rate used in the ramp up leading to the recorded steady state.

state experiments, the frame rates used allowed all temporal frequencies in the flow to be resolved.

The  $2176 \times 16$  pixel<sup>2</sup> images were horizontally averaged to form an axial intensity profile for each instance. All such profiles were compiled into a matrix, or flow map, showing the evolution of the intensity profile over time or any time dependent parameter, such as Re (see e.g figure 6 b). In a second step, the flow maps were divided into segments of  $N_c = 256$  columns (successive snapshots), with a 50% overlap, in order to calculate the average Fast Fourier Transform (FFT) for each row (i.e. each axial location) in each segment. All the averaged spectra were subsequently compiled to form a frequency map (see e.g. figure 6 c, (Cagney & Balabani 2019b)). This map shows the evolution of the temporal frequencies of the flow as a function of time or Re. On frequency maps, a clear ridge may appear for regions with  $f = f_\Omega/2\pi$  (see figure figure 6 c), with fainter additional ridges at  $f = k \times f_\Omega/2\pi$ . These ridges arise from the ability of the visualisation method to detect the rigid body rotation frequency of the inner cylinder and its harmonics, and should not be interpreted as fluid flow frequencies.

In this work, the focus is on ramp up experiments:  $\Omega$  was increased at a constant rate,  $d\Omega/dt$ , up to a maximum rotation speed  $\Omega_{max}$ , which led to an increase in the Reynolds number up to  $Re_{max} \simeq 300$ . For shear-thinning fluids, Re was computed using an effective viscosity  $\mu(\dot{\gamma})$  derived from Carreau fittings, and thus increases non-linearly with  $\Omega$ . The flow maps resolution in terms of Reynolds number is quantified by the ratio  $1/\Delta Re$ , reported in table 2, where  $\Delta Re$  is the average Reynolds number variation between two successive images. The (Newtonian) non-dimensional acceleration rate is defined as

$$\Gamma_0 = \frac{dRe}{dt^*} = \frac{\rho^2 r_i d^3}{\mu^2} \frac{d\Omega}{dt}, \quad (2.4)$$

where  $t^* = t/t_v$  is the time divided by the viscous time-scale. This acceleration rate must be kept low (typically  $\Gamma_0 < 1$ ) to ensure that flow states are independent of the cylinder acceleration, i.e. that the ramp up can be treated as a quasi-static process (Dutcher & Muller 2009). In appendix A of the present work, we present an investigation of the effects of acceleration in our experimental conditions, achieved by performing specific experiments in which the acceleration rate was varied over three decades. Based on the results of this investigation, acceleration rates used for the main set of experiments (section 3) were selected. Values of ramp up parameters are reported in table 2. Values of the Nahme-Griffith number were estimated to be of order  $10^{-1}$  at most for all working fluids at all shear rates (see supplementary information), thus indicating that viscous heating effects are negligible (White & Muller 2002b,a).

For shear-thinning fluids, El and  $\Gamma_0$  were not exactly constant during the ramp up process as the viscous time scale depends on the rotation speed in a non-linear fashion (Dutcher & Muller 2013; Cagney *et al.* 2020). In a Carreau fluid,  $n_e$  also varies with the shear rate, which depends on the rotation speed. Thus reference values for each run, taken as the average over the Reynolds range from 20 to  $Re_{max}$  are also displayed in table 2. Such run-averaged values are noted by overbar symbols (e.g.  $\bar{n}_e$  or  $\bar{El}$ ). The reference value for  $\Gamma_0$  was chosen as the maximum one and simply noted  $\Gamma_0$  hereafter for the sake of simplicity.

Additionally, some ‘‘steady state’’ experiments were performed in order to visualise specific flow states for longer times. For this type of experiment, the cylinder was first accelerated at  $d\Omega/dt$  corresponding to a maximum acceleration rate  $\Gamma_0$  until the targeted rotation speed/Reynolds number was reached, and the acquisition started. Details of such

experiments are provided in table 3. The absence of polymer degradation was verified for all fluids by comparing the steady and oscillatory shear rheological characterisation made before and after the flow visualisation experiments. An example of comparison between pre-experiment and post-experiment rheological characterisations is available in supplementary information for the XG2000-50 case (chosen as the most critical in terms of degradation probability, with its high polymer contribution to the viscosity and the strong shear-rate at which it is employed during experiments).

As a final note for this section, it should be mentioned that instabilities and flow transition in viscoelastic fluids are often found to be hysteretic and strongly subcritical (Martínez-Arias & Peixinho 2017; Groisman & Steinberg 1996). If one were to characterise the nature of the bifurcations, ramp-down experiments (decreasing inner cylinder rotation speed) would be needed. From the results of Martínez-Arias & Peixinho (2017), there is no reason to expect shear-thinning to completely suppress hysteretic behaviours. It would yet be of great interest to see how the conclusions of the present study on shear-thinning mediation of elasto-inertial flow patterns apply to flow states encountered specifically during ramp-down protocol only, such as diwhirls described in Groisman & Steinberg (1996); Lange & Eckhardt (2001); Martínez-Arias & Peixinho (2017).

### 3. Results

#### 3.1. Overview of flow transitions

An overview of all flow states and ramp up experiments is first presented. Each experiment starts from  $Re = 0$  and  $Re$  is progressively increased. Flakes align with dominant flow structures, reflecting light more or less intensely depending on their orientation, allowing to capture various transitions to CF, TVF, WTVF, RSW, EIT, and SVF. A time-space diagram, at constant  $Re$ , is provided for each flow state in figure 4 a to f. In TVF, SVF or WTVF, the flakes align with the (wavy/spiraling) Taylor vortices, giving rise to a band like structure (figure 4 a) that may be seen oscillating (figure 4 b) or travelling (figure 4 e) for WTVF and SVF, respectively. In RSW, the base TVF structure is still visible but additional patterns appear due to the local alignment of the flakes with axial elastic waves (figure 4 c). In EIT, the random alignment of flakes with a set of various spatial flow structures translates into a chaotic intensity signal and space-time plot (figure 4 d). Note that in CF, flakes are all aligned in the azimuthal direction, and the resulting time-space diagram is homogeneously gray (figure 4 f).

Examples of spatial and temporal FFT (denoted as  $FFT_s$  and  $FFT_t$ ) of the space-time plots are shown in figure 4 g and h, as a function of the spatial wavelength and temporal frequency, respectively. These are computed along vertical and horizontal lines of subplots from figure 4, respectively. The location of the peak(s) in these spectra, if present, can be used to determine the major spatial wavelength(s)  $\lambda$  and temporal frequency frequency(ies) of the flow.

Figure 5 a) shows the succession of flow states encountered during several ramp up processes (only one experiment per working fluid is shown for the sake of readability), in a 3D space of elasticity, shear-thinning ( $1-\bar{\eta}_e$ ) and reduced Reynolds number ( $Re/Re_0$ ), where  $Re_0 = 107$  is the critical  $Re_c^{TVF}$  Reynolds number for the CF to TVF transition for Newtonian fluids in the present setup. A table summarizing all critical Reynolds numbers for flow transitions is available in the supplementary information file. The results of Cagney *et al.* (2020) have also been rescaled and added to the graph as dashed lines with the same colour code. Figures 5 b and 5 c are projections of figure 5 a in  $(El, Re)$  and  $(1-\bar{\eta}_e, Re)$  planes, respectively. The transition patterns are also summarized in table 2.

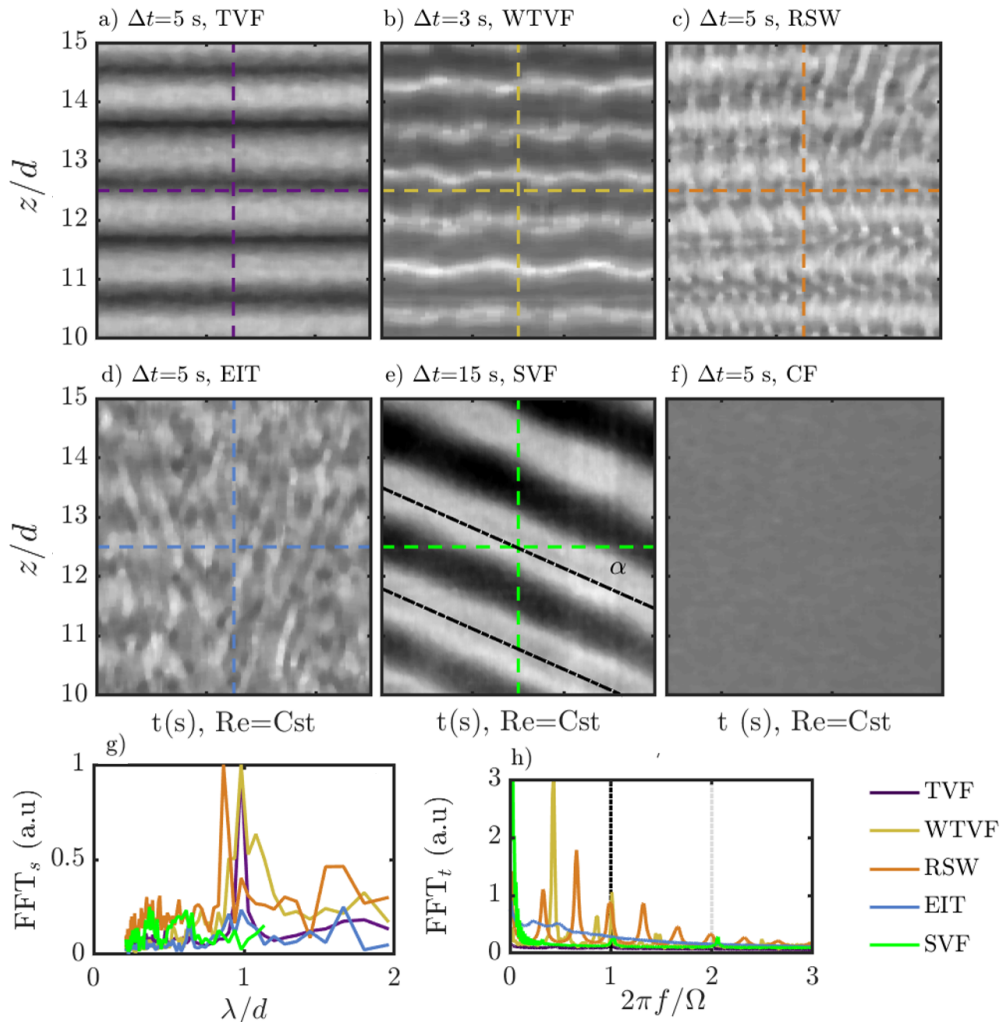


Figure 4: Illustrative panel of observed flow maps and flow states. (a-f) are time-space diagrams on  $\Delta t$  intervals of 3 to 15 s spanning the  $10 < z/d < 15$  vertical region. a) N72,  $Re=120$  b) N72,  $Re=250$  c) P500-72,  $Re=110$  d) P500-72,  $Re=150$  e) XG2000-50,  $Re=52$  f) P500-72,  $Re=50$ . g) and h) illustrate typical spatial and temporal spectra,  $FFT_s$  and  $FFT_t$ , obtained by FFT processing along the vertical and horizontal dashed lines in (a-e), respectively.

379 No clear trend appears from the 2D projections: several regimes may co-exist in some  
 380 regions of the plots. For example at  $Re = 2 \times Re_0$  and  $El \sim 0.1$ , the P500-72 experiment  
 381 features EIT while the XG200-50 experiment is in the WTVF state for similar inertia  
 382 and elasticity (figure 5 b). Similarly, at  $Re = 2 \times Re_0$  and for  $1 - n_e \sim 0.3$ , XG1000-72  
 383 experiments feature EIT while XG200-50 is in the WTVF state, while at equivalent levels  
 384 of inertia and shear-thinning (figure 5 c). It is therefore necessary to consider all three  
 385 parameters to distinguish preferential regions for each flow state in the three dimensional  
 386 parameter space, as done in figure 5 a). WTVF can be found at high  $Re/Re_0$ , but only

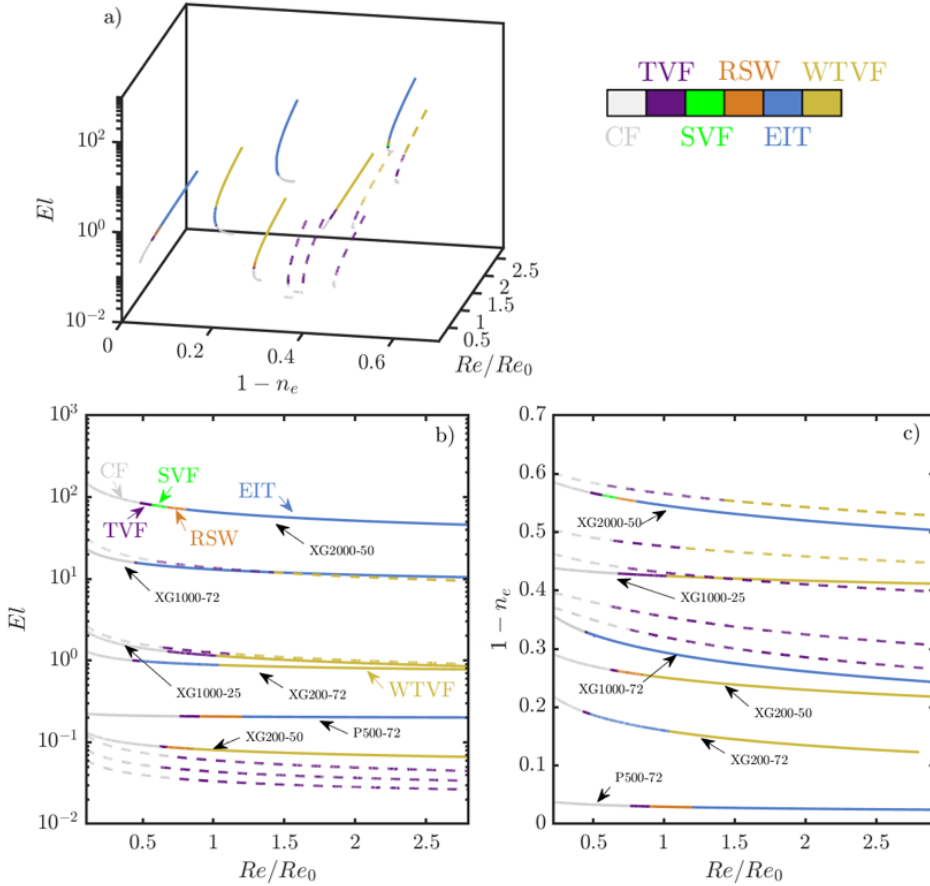


Figure 5: Summary of experiments in  $(Re/Re_0, 1 - n_e, El)$  (a),  $(Re/Re_0, El)$  (b) and  $(Re/Re_0, 1 - n_e)$  (c) parameter spaces. Each path corresponds to a single ramp up experiment. Each flow state is associated with a line colour according to the legend (colours online). Full lines report experiments from the present work, and dashed lines experiments from Cagney *et al.* (2020), performed in similar conditions (polymer batch, geometry, ramp up protocol, flow visualisation method) on xanthan gum samples at various concentrations dissolved in a 25% glycerol in water solvent.

387 for intermediate elasticity. Conversely, EIT requires either strong elasticity or negligible  
 388 shear-thinning to develop. The existing conditions of different flow states based on the  
 389 rheological and inertial parameters are detailed and discussed in the rest of section 3.

390

### 3.2. Non shear-thinning cases

#### 391 3.2.1. Newtonian fluid

392 In the Newtonian reference case, the expected CF-TVF-WTVF transition pattern is  
 393 retrieved, as illustrated in figure 6 with the N72-1 experiment. Prior to the onset of any  
 394 instability, Ekman vortices (Cole 1976) develop at the top and bottom of the cylinder (see  
 395 e.g. figure 6 b), top and bottom). The transition from CF to a band-like TVF structure  
 396 can be clearly seen by a jump in the rms value of the z-intensity profile 6 a, denoted

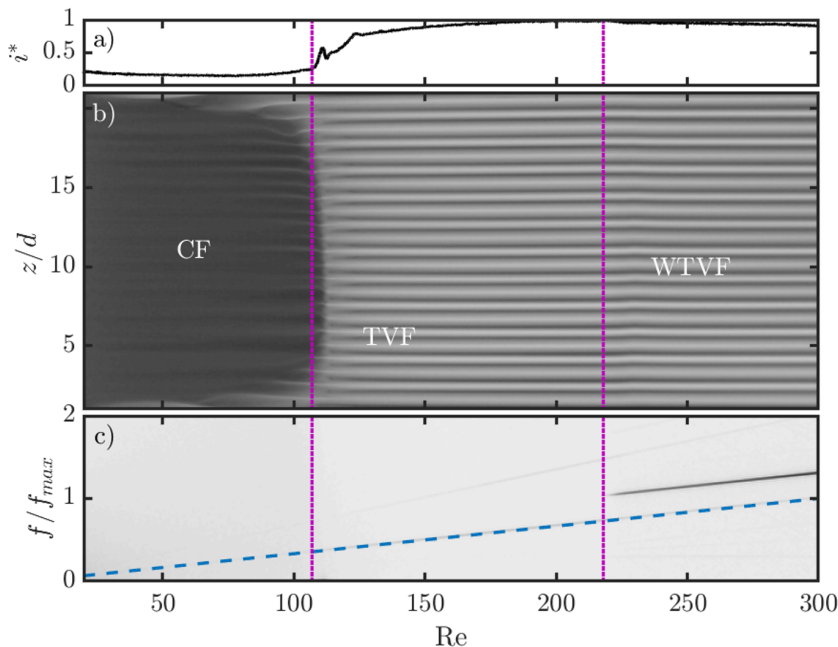


Figure 6: Intensity signal (a), flow map (b) and frequency map (c) for the N72-1 experiment ( $\overline{El}=0$ ,  $\overline{n}_e=1$ ). In a) and all subsequent similar figures,  $i^*$  is the root mean square gray level intensity of sub-plot b) along the  $z/d$  dimension, scaled by its maximum value on the  $Re$  range. The dashed line on sub-figure c) denotes the inner cylinder rotation frequency  $f_\Omega$ .  $f_{max}$  is the rotation frequency corresponding to  $\mathcal{R}]_m ax$ . Vertical dotted lines shows the transitions between flow regimes.

397  $i^*$ . The CF to TVF transition occurs at  $Re_c^{TVF} = 107 = Re_0$  and the transition from  
 398 TVF to WTVF occurs at  $Re_c^{WTVF} = 218 = 2.03 \times Re_0$ . The latter, while difficult to  
 399 observe on the flow map (figure 6 b) due to a weak spatial amplitude, is clearly seen on  
 400 the frequency map (6 c) when an additional frequency ridge appears. Both results are  
 401 consistent with the values reported in the literature (see for example Dutcher & Muller  
 402 (2009); Cagney & Balabani (2019b); Ramesh *et al.* (2019)), ranging from 80 to 120 and  
 403 170 to 450 respectively. The wavelength of TVF is  $\lambda = 0.89d$ . The critical wavy frequency  
 404 at the onset of the WTVF is  $f_w = 1.02 \times f_{max} = 1.40 \times \frac{\Omega}{2\pi}$ .

### 405 3.2.2. Boger fluid

406 In the Boger fluid case (P500-72), the transition pattern observed is CF-TVF-RSW-  
 407 EIT (see figure 7). It is consistent with transitions reported in the literature for moderate  
 408 or high elasticity fluids (Groisman & Steinberg 1996; Schaefer *et al.* 2018). The onset of  
 409 TVF happens at lower  $Re$  than in the Newtonian case,  $Re_c^{TVF} = 97 = 0.90 \times Re_0$ . Elastic  
 410 waves (RSW) appear soon and abruptly after the onset of the TVF state, at  $Re_c^{RSW} =$   
 411  $103 = 0.96 \times Re_0$ , as several horizontal ridges become visible in the frequency map  
 412 (figure 7 c). These correspond to elastic waves, the frequency of which is not correlated  
 413 to the Reynolds number but rather to the constant elastic number, through the elastic  
 414 time scale (see Gillissen (2019); Lacassagne *et al.* (2020)). As a point of comparison,  
 415 Dutcher & Muller (2013) reports transition to TVF at  $Re_c^{TVF}/Re_0 = 1.07$  and to RSW  
 416 at  $Re_c^{RSW}/Re_0 = 1.13$  in moderately elastic Boger fluids ( $El = 0.1 - 0.2$ ). The apparent

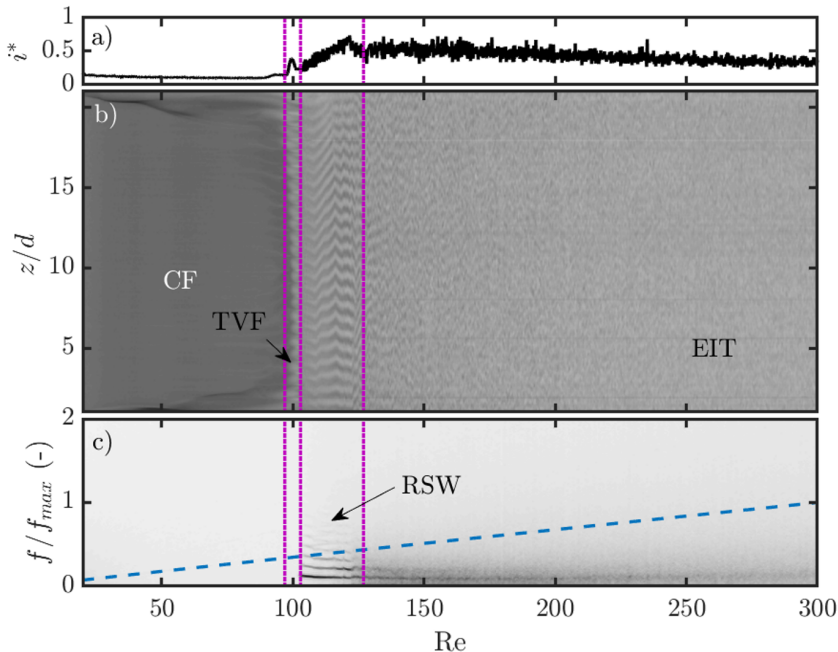


Figure 7: Intensity signal (a), flow map (b) and frequency map (c) for the P500-72-3 experiment ( $\overline{El}=0.19$ ,  $\overline{n}_e=0.96$ ). The dashed line on sub-figure c denotes the inner cylinder rotation frequency. Vertical dotted lines denote the transitions between flow regimes.

417 spatial wavelengths are  $\lambda = 0.82d$  and  $\lambda = 0.89d$  in TVF and RSW states, respectively,  
 418 while Dutcher & Muller (2013) reported  $\lambda \approx 1.6d$  in both states. The flow finally becomes  
 419 increasingly disordered with  $Re$ , and quickly transitions to EIT at  $Re$  values for which it  
 420 would be laminar under purely inertial conditions.

421

### 3.3. Shear-thinning dominated fluids

422 In the highly shear-thinning ( $\overline{n}_e = 0.5766$ ) XG1000-25-1 case, a Newtonian-like transition  
 423 pattern is observed: CF-TVF-WTVF (figure 8). A similar behaviour has been  
 424 reported in several other studies where the fluid exhibited a non-negligible shear-thinning  
 425 behaviour and negligible to moderate elasticity (Crumeyroille *et al.* 2002; Cagney &  
 426 Balabani 2019*b,a*; Cagney *et al.* 2020). Here it occurs despite the elastic number ( $\overline{El} =$   
 427 1.2) being approximately five times that of the fluid discussed in the previous section.  
 428 Boger fluids of equivalent elastic number in the present experimental set-up are expected  
 429 to exhibit elastic flow features such as RSW or transition to EIT, as suggested by  
 430 experiment reported above (section 3.2.2). The absence of these in the flow map of  
 431 figure 8 suggests that elastic effects are suppressed by shear-thinning. The CF to TVF  
 432 transition occurs at  $Re_c^{TVF} = 72 = 0.67 \times Re_0$ . The flow is thus destabilised by combined  
 433 shear-thinning and elasticity. The spatial wavelength of TVF is  $\lambda = 0.99$ , which is, as  
 434 expected, slightly larger than that for the Newtonian case (Escudier *et al.* 1995; Cagney  
 435 & Balabani 2019*b*). The WTVF arises at  $Re_c^{WTVF} = 109 = 1.01 \times Re_0$ , again much  
 436 sooner than in the Newtonian case. Moreover, at the onset of WTVF, the wave frequency  
 437 is lower than the inner rotation frequency ( $f_w = 0.432 \times \frac{\Omega}{2\pi}$ ) while it is higher in the

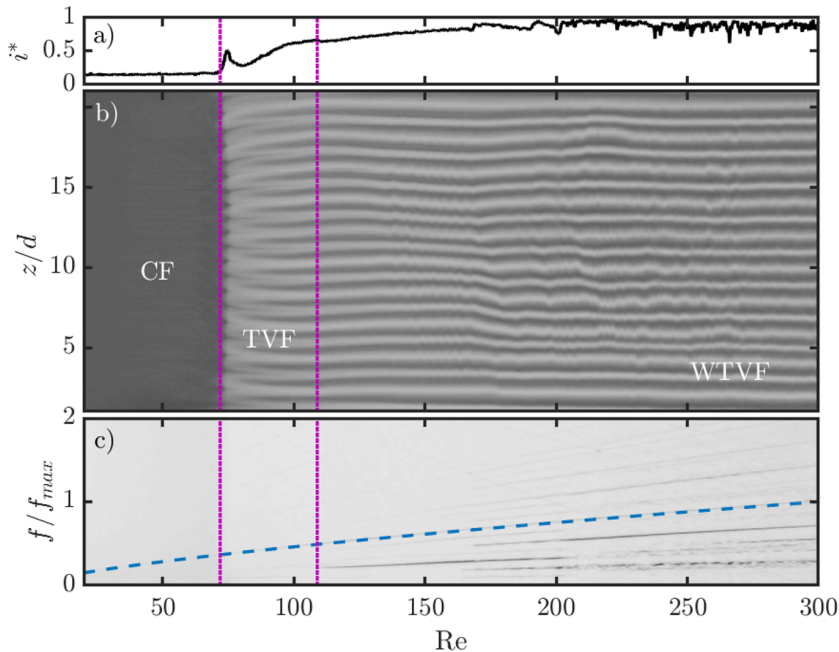


Figure 8: Intensity signal (a), flow map (b) and frequency map (c) for the XG1000-25-1 experiment ( $\overline{El}=1.2$ ,  $\overline{n}_e=0.58$ ). The dashed line on sub-figure c denotes the inner cylinder rotation frequency. Vertical dotted lines denote the transitions between flow regimes. Note that the rotation frequency detected varies non-linearly with  $Re$ , due to the shear-thinning behaviour (Cagney & Balabani 2019b).

438 Newtonian case. Finally, the complexity of the WTVF is enhanced, with ridges appearing  
 439 and disappearing as  $Re$  increases.

440

### 3.4. Elasticity dominated fluids

441 By keeping the same polymer at the same concentration (XG 1000 ppm) but simply  
 442 increasing the solvent viscosity (XG1000-72-2 experiment), it is possible to produce a  
 443 fluid of much higher elasticity ( $\overline{El} = 13$ ) and weaker shear-thinning ( $\overline{n}_e = 0.71$ ). This  
 444 fluid exhibits strikingly different patterns (figure 9). The flow abruptly transitions from  
 445 CF to EIT, which is the typical behaviour of highly elastic fluids (Groisman & Steinberg  
 446 1996). This transition is easily detected from the abrupt jump in intensity rms signal  
 447 (figure 9 a). No specific frequency can be identified in the flow map, as was also the  
 448 case in the Boger fluid (figure 7) in the EIT state. The CF-EIT transition occurs at  
 449  $Re_c^{EIT} = 47 = 0.44 \times Re_0$ , which is in line with the results reported by Groisman &  
 450 Steinberg (1996): elasticity strongly destabilizes the base Couette flow. While the latter  
 451 is a well known result, the very different transition sequences in figures 8 and 9 constitute  
 452 an interesting novelty of this study. Depending on the relative degrees of shear-thinning  
 453 and elasticity dictated by the solvent properties, the flow of the same polymer at the same  
 454 concentration may exhibit completely different hydrodynamic behaviours. Observations  
 455 thus suggest that not only elasticity destabilises the flow, but it can also induce various  
 456 hydrodynamic regimes by tuning the relative degrees of shear thinning and elasticity.



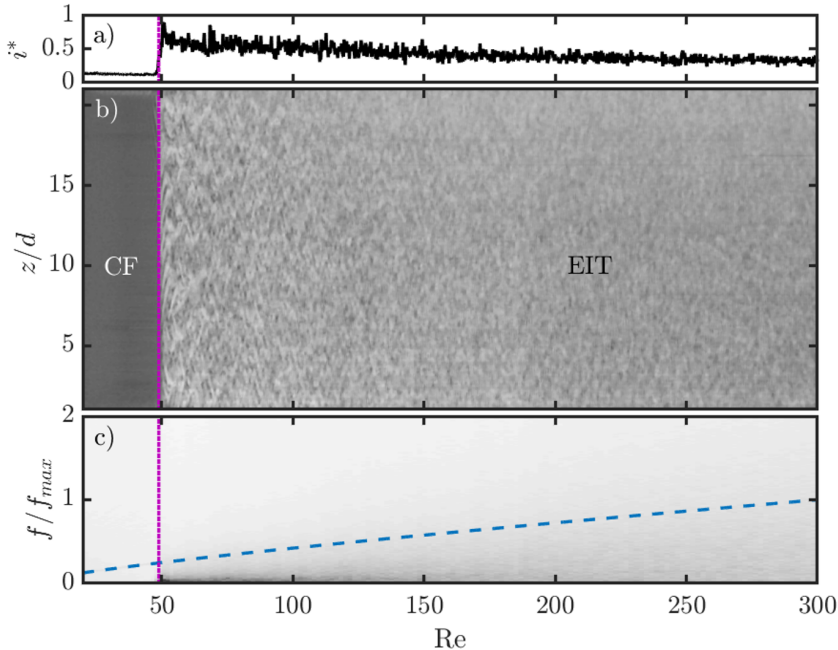


Figure 9: Intensity signal (a), flow map (b) and frequency map (c) for the XG1000-72-2 experiment ( $\overline{El}=13$ ,  $\overline{n}_e=0.71$ ). The dashed line on sub-figure c denotes the inner cylinder rotation frequency. Vertical dotted lines denote the transition from CF to EIT. Note that the rotation frequency detected varies non-linearly with  $Re$ , due to the shear-thinning behaviour, but this non-linear trend is weaker than in figure 8 c), the shear-thinning index being here closer to 1.

457

### 3.5. Moderate shear-thinning and elasticity

458

Through changes in both solvent viscosity and polymer concentration, we can then keep a similar flow index ( $\overline{n}_e \approx 0.8$ ) and adjust the elasticity to be equivalent to that in the Boger fluid ( $\overline{El} \approx 0.1$ , figure 7, sub-section 3.2.2)), in order to probe the flow transitions in the moderate elasticity, moderate shear thinning regime of the parameter space (figure 5).

461

462

463

464

465

466

467

468

469

470

471

472

473

474

475

476

The behaviour (illustrated in figure 10, XG200-50-3 ramp up experiment) approaches that of a fluid dominated by shear-thinning, with a Newtonian-like transition pattern, as shown in figure 8. The only notable difference is the existence of an intermediate RSW state between the TVF and WTVF states. The CF to TVF transition occurs at  $Re_c^{TVF}/Re_0 = 0.62$ . RSW waves appear at  $Re_c^{RSW}/Re_0 = 0.67$  and completely disappear after  $Re_c^{WTVF}/Re_0 = 0.83$ . This RSW pattern bears some similarities with that exhibited by the Boger fluid (figure 7). However, shear-thinning seems to modify the nature of the RSW waves by enhancing their dependency on inertia, since the ridges are not completely  $Re$ -independent (figure 10 c).

Instead of EIT (as occurs for a Boger or elasticity dominated fluid), the flow transitions back to WTVF with increasing  $Re$ . The WTVF state exists at  $Re$  values lower than in the Newtonian case ( $Re \simeq 100$ ), in line with the results for Newtonian-like shear-thinning fluids described in section 3.3. In order to investigate this specific RSW to WTVF transition further, steady state experiments were performed on this fluid at three

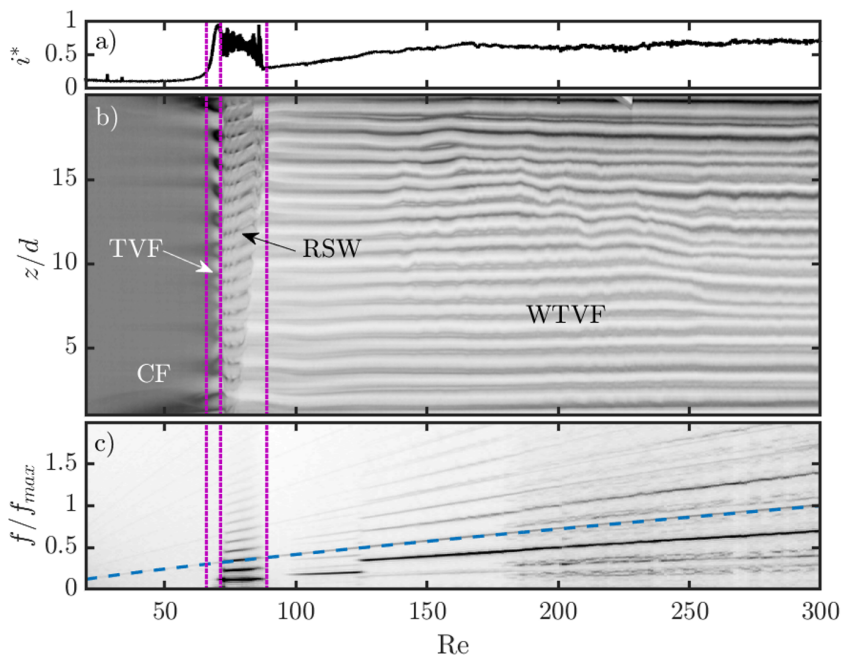


Figure 10: Intensity signal (a), flow map (b) and frequency map (c) for the XG200-50-3 experiment ( $\overline{E}|=0.14$ ,  $\overline{n}_e=0.73$ ). The dashed line on sub-figure c denotes the inner cylinder rotation frequency. Vertical dotted lines denote the transitions between flow states. Note that the rotation frequency detected varies non-linearly with Re, due to the shear-thinning behaviour (Cagney & Balabani 2019b).

477 different Re values: Re = 76 (S1), Re = 114 (S2) and Re = 198 (S3) (see table 3). These  
 478 are described in figure 11.

479 The S1 case (figure 11 a and d) displays a RSW pattern in which the base TVF  
 480 structure is still visible, but periodic patterns are very pronounced. The frequency  
 481 spectrum (figure 11 h) clearly shows multiple peaks, with the highest energy peak found  
 482 at  $f = 0.33 \times \frac{\Omega}{2\pi}$ . The S2 case (figure 11 b and e) lies between S1 and S3, with an  
 483 evident WTVF structure; however, darker and whiter spots can be detected along given  
 484 horizontal lines (figure 11 e), indicating persisting RSW waves. The S3 case (figure 11  
 485 c and f) shows a WTVF pattern similar to other reported shear-thinning WTVF states  
 486 (figure 8, Cagney & Balabani (2019b)). The wavy frequency is lower than the inner  
 487 cylinder frequency ( $f_w = 0.750 \times \frac{\Omega}{2\pi}$  at Re = 198, or  $f_w = 0.689 \times \frac{\Omega}{2\pi}$  at Re = 150 in  
 488 figure 10 c). Multiple secondary peaks are visible, indicating a complex wavy behaviour.  
 489 S2 and S3 share a common peak at the same  $f_w$  value when the frequency is scaled by  $\Omega$   
 490 (figure 11 h). This peak is thus characteristic of an inertial flow feature, namely, WTVF.  
 491 On the other hand, the lower frequency peak found in S1 at  $f = 0.33 \times \frac{\Omega}{2\pi}$  is retrieved on  
 492 S2 and S3 but progressively drifts towards higher frequencies with increasing Re when the  
 493 same scaling is used. This suggests that this other peak is not associated with inertia, but  
 494 rather correlates with the elastic wave frequency (see figure 7, Lacassagne *et al.* (2020)).  
 495 This elastic feature ( $f_w$  scaling with  $t_e^{-1}$ ) progressively yields to inertia ( $f_w$  scaling with  
 496  $\Omega$ ), as the flow gradually transitions from RSW to WTVF. The fact that the RSW ridges  
 497 are not perfectly horizontal in the frequency maps suggests that, in shear-thinning fluids,  
 498 both inertial and elastic effects are involved in the RSW pattern.

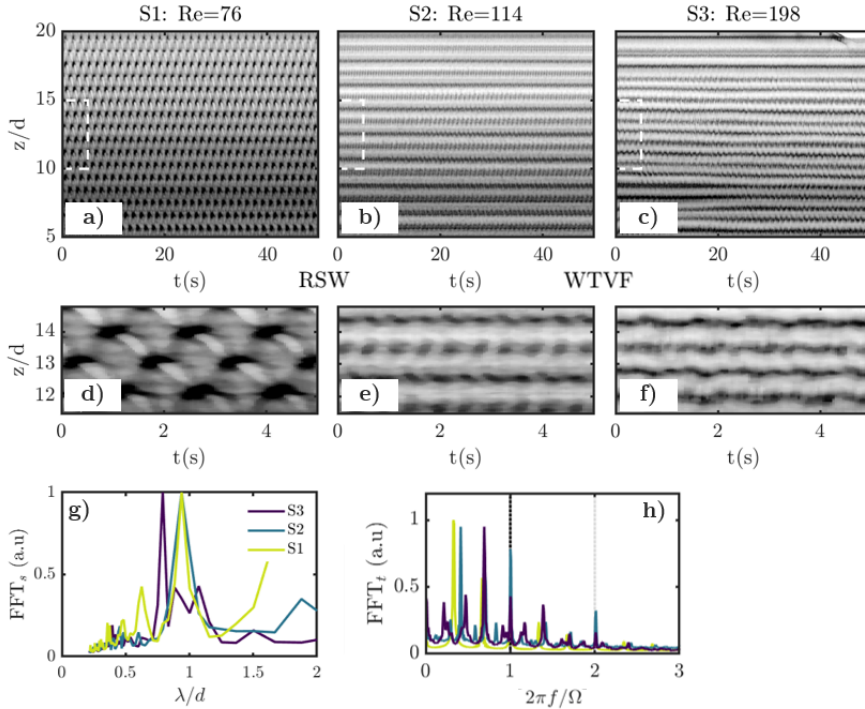


Figure 11: Steady state recordings at constant  $Re$  of successive RIB and WTVF states for the XG200-50 case ( $\overline{El}=0.14$ ,  $\overline{n}_e=0.73$ ). (a-c) Time-space diagrams over 50 s time spans. (d-f) Close-ups of the same flow maps on the first 5 seconds and in the central region (dashed rectangles). g) Spatial spectrum and h) temporal spectrum of the three steady state experiments.

499 Further insight is brought by slightly shifting the fluids properties towards a more  
500 elastic, less shear-tinning case (XG200-72,  $\overline{El}=0.88$ ,  $\overline{n}_e=0.85$ ). The transition pattern is  
501 then CF-TVF-RSW-EIT-WTVF, with an additional EIT state appearing between RSW  
502 and WTVF. The CF to TVF transition occurs at  $Re_c^{TVF}/Re_0 = 0.43$ . RSW develops  
503 over a very limited  $Re$  range, from  $Re_c^{RSW}/Re_0 = 0.48$ , quickly transitioning to EIT,  
504 and then smoothly to WTVF at  $Re_c^{WTVF}/Re_0 = 1.0$ . At  $Re = 150 = 1.4 \times Re_0$  where  
505 the wavy frequency ridge is clearly visible on the frequency map (figure 12 c), the wavy  
506 frequency is  $f_w = 0.451 \times \frac{\Omega}{2\pi}$ .

507 This other fluid thus displays an elastic transition sequence(CF-TVF-RSW-EIT) until  
508 a sufficient amount of inertia ( $Re$ ) is reached, and the flow re-transitions to a Newtonian-  
509 like behaviour, yet marked by shear-thinning. It is thus an extension of the previous case  
510 (XG200-50, figure 10) where elasticity plays a greater role in determining the nature  
511 of the transitions, as expected from the variations in rheological properties between  
512 the two fluids. It also leads to a counter-intuitive observation: the complexity of the  
513 flow and degree of chaos, induced by elasticity, can be reduced when increasing inertia  
514 together with shear-thinning. This intriguing behaviour cannot be attributed to polymer  
515 degradation, as rheological characterisation before and after confirmed the integrity of  
516 the polymer solutions. A possible explanation is the existence of an underlying damping  
517 mechanism of elastic waves with increasing inertia ( $Re$ ).

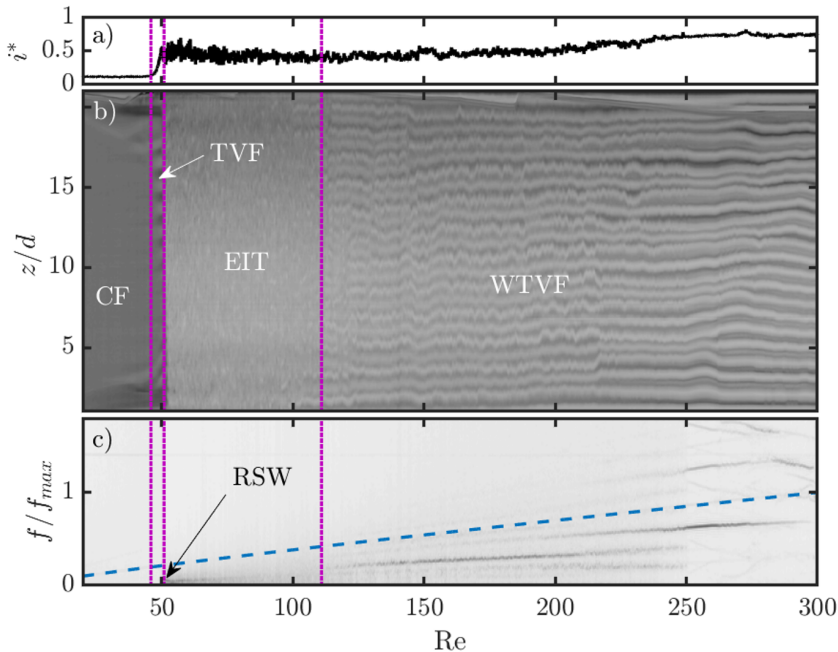


Figure 12: Intensity signal (a), flow map (b) and frequency map (c) for the XG200-72-1 experiment ( $\overline{E}l=0.88$ ,  $\overline{n}_e=0.85$ ). The dashed line on sub-figure c denotes the inner cylinder rotation frequency. Vertical dotted lines denote the transitions between flow states. Note that the rotation frequency detected varies non-linearly with  $Re$ , due to the shear-thinning behaviour (Cagney & Balabani 2019b).

518 Shear-thinning may compete with elasticity to condition the existence of elastic waves  
 519 of flow patterns in the fluid (as previously observed by comparing figures 8 and 9), even to  
 520 the point of re-laminarising the flow (figures 10, 12). Mild shear-thinning with moderate  
 521 inertia allows elastic waves to exist, but high shear-thinning with moderate inertia (see  
 522 XG1000-25 case), or mild shear-thinning with higher inertia (XG200-50, XG200-72) do  
 523 not.

### 524 3.6. Highly shear-thinning, highly elastic fluids

525 Experiments with a highly elastic and shear-thinning fluid (XG2000-50-2,  $\overline{E}l = 74$ ,  
 526  $\overline{n}_e = 0.56$ ) are reported in figure 13. The flow transition pattern is mostly elastic-like,  
 527 with the final state being EIT (for  $Re < 300$ ). It is yet different from that of a Boger  
 528 fluid, with an additional SVF (Spiral Vortex Flow) pattern appearing between TVF and  
 529 RSW. The transition sequence is thus CF-TVF-SVF-RSW-EIT. As expected from the  
 530 strong elasticity and shear-thinning properties of the fluid, the CF destabilises at low  $Re$   
 531 values, and the onset of TVF occurs at  $Re_c^{TVF} = 37 = 0.34 \times Re_0$ . EIT is reached at  
 532  $Re_c^{EIT} = 78 = 0.73 \times Re_0$ . The intermediate flow states therefore occur within a short  
 533 Reynolds span. The transitions to RSW and EIT are close in  $Re$  values, which compares  
 534 well to the behaviour observed previously in the XG200-72 experiment (section 3.5, figure  
 535 12).

536 The additional SVF flow state corresponds to Taylor vortices spiralling and travelling  
 537 along the axial direction, which translates on the flow maps as slanted dark and white  
 538 stripes, not showing any particular temporal signature on the frequency map. The

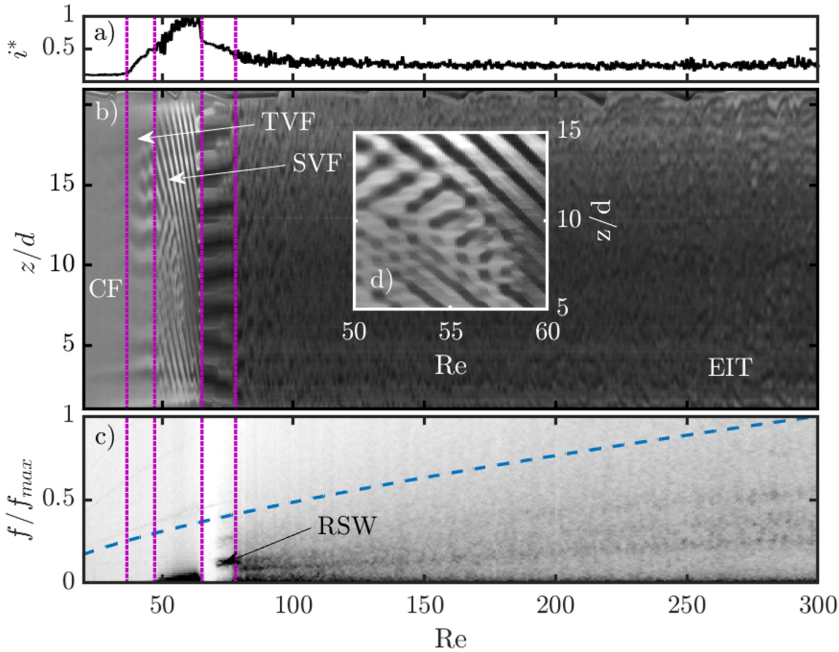


Figure 13: Intensity signal (a), flow map (b) and frequency map (c) for a highly elastic, highly shear-thinning fluid (XG2000-50-2 experiment,  $\overline{El}=74$ ,  $\overline{n}_e=0.56$ ). The dashed line on sub-figure c denotes the inner cylinder rotation frequency. Vertical dotted lines denote the transitions between flow states. Note that the rotation frequency detected varies non-linearly with  $Re$ , due to the shear-thinning behaviour. d) is a zoom of b) in the SVF state.

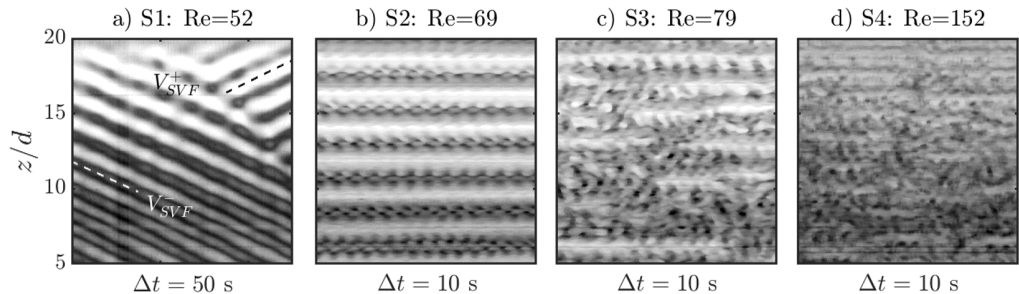


Figure 14: Steady state experiments in the SVF (S1), RSW (S2) and EIT (S3, S4) states, shown on  $\Delta t$  intervals (horizontal axis) (S1 interval is larger in order to better describe the SVF state). Superscripts “-” and “+” in S1 denote upward and downward spiralling velocities, respectively.

539 existence of such a flow state has been reported in elastic fluids (including the experiments  
 540 of Baumert & Muller (1997), linear stability analysis of Avgousti & Beris (1993)), solid  
 541 particle suspensions (Ramesh *et al.* 2019; Ramesh & Alam 2020), but also Newtonian  
 542 fluids with counter-rotating outer cylinder (Andereck *et al.* 1986). Sudden changes of the  
 543 spiralling propagation direction may occur and give rise to a similar flow state called the  
 544 Inter-penetrating Spiral Vortex Flow (ISVF) (Ramesh & Alam 2020; Baumert & Muller  
 545 1997). In the recent works by Elçiçek & Güzel (2020*b,a*) SVF (sometimes coexisting

with TVF) has also been observed in shear-thinning (possibly also elastic) XG solutions. Remarkably, SVF and ISVF have been found to coexist with RIB states under certain conditions (Ramesh & Alam 2020). Indeed, RIB is actually the flow pattern resulting from the interactions between up-going and down-going stationary spirals of similar amplitudes. Latrache and co-workers (Latrache *et al.* 2016) have shown that in shear-thinning and viscoelastic PEO solutions, a local reduction in the amplitude of either of the two spirals led to spatial defects, the multiplication of which was a mechanism for the transition to EIT. A subregion of the flow map in figure 13 b) in the (I)SVF state is shown in detail in figure 13 d). SVF can be found to propagate either upwards or downwards. In highly shear-thinning XG solutions, it thus appears that one of the spirals can be completely suppressed, either on the full height of the cylinder (figures 13 b), 13 d), 14 S1), or locally (Elçiçek & Güzel 2020*b*). SVF or ISVF could thus be thought of as an alternative version of the RIB state, whereby shear-thinning combined with elasticity prevent spirals from co-existing everywhere in the gap.

Complementary steady state experiments have been performed and reported in table 3 and figure 14. This allows the spiral travelling speed to be computed for a constant  $Re = 52$  value:  $V_{SVF} = d \times \alpha$ , where  $\alpha$  (expressed in  $s^{-1}$ ) is the slope of iso-intensity lines on a time-(normalized) space flow map (time *versus*  $z/d$ , figures 4 e), 14 a)). It is found that  $V_{SVF}^- = -0.84 \text{ mm.s}^{-1}$  in the downward spiralling section of the steady state experiment (figure 14, S1,  $t < 40 \text{ s}$ ,  $z/d < 15$ , lower dashed line). In the upper right corner of figure 14, S1, an upward spiralling region is observed, with  $V_{SVF}^+ = 0.90 \text{ mm.s}^{-1}$  (dark dashed line). The very close magnitude of these two velocities suggests that SVF and RIB spirals are related, but that SVF corresponds to a bistable state, where a wave of given velocity may travel in either direction, while the RIB state requires both waves to coexist.

The steady state experiment in the RSW state (at  $Re = 69$ , sub-figure 14 b), shows a pattern similar to that of the mild shear-thinning and elastic case XG200-50 in figure 11. With increasing  $Re$ , RSW state becomes increasingly disordered (figure 14 S3) and ultimately transitions to EIT (S4). In figure 15, the visualisation of figure 14 S3) is extended to a larger time span. Base Taylor vortices are crossed by multiple RSW waves, and the occurrence of several merge-split events and associated drifting of such base Taylor vortices are observed, leading to increased chaotic behaviours. Some merge-split and drifting features are indicated in figure 15 by dashed circles and lines respectively. This Merge-Split transition (MST) is a mechanism of transition to EIT in elastic, Boger fluids (Lacassagne *et al.* 2020), and it appears that it also applies here in the case of a highly elastic but also shear-thinning fluid.

Finally, from the steady state experiment above (figure 14), two-dimensional space-time spectra can be computed as a means to probe the spatio-temporal dynamics of EIT, in this case in a shear-thinning fluid. In the RSW state, a spatial peak exists at  $\lambda/d \sim 1$ , due to the base TVF (figure 16 a). In the temporal dimension, several clear peaks are identified, the most energetic found at frequencies much lower than the rotation frequency of the inner cylinder (figures 7 c, 10 c, 11 h, (Lacassagne *et al.* 2020)).

In the transitional RSW-EIT state (figure 16 b) several peaks can be seen in the temporal spectra, albeit broader. The spatial peak corresponding to TVF is reduced in relative amplitude, and the most dominant one is found for  $\lambda/d < 1$ . The spatial structure of the flow is no longer dominated by the Taylor-Vortex wavelength, but by RSW waves of smaller wavelengths. Ultimately, EIT (figure 16 c) displays smoother, broadband spectra of multiple spatial and temporal scales, which correspond well to the common definition of turbulence (Fenstermacher *et al.* 1979; Dutcher & Muller 2013; Liu & Khomami 2013).

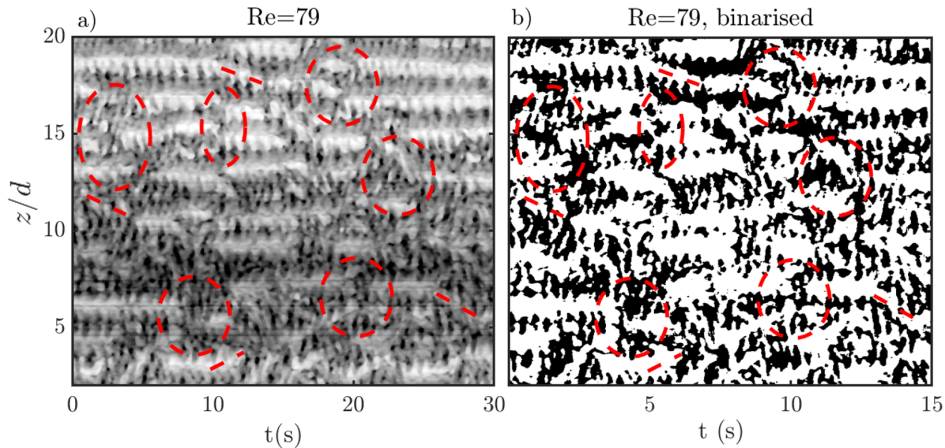


Figure 15: Steady state experiment (30 s) showing the transitional stage between RSW and EIT in highly elastic and shear-thinning XG2000-50 fluid, at  $Re = 79$ . a) Reflected intensity, b) binarized intensity map. Some of the numerous merging and splitting events of Taylor-Vortices are highlighted by dashed circles, and the associated vortex drifting by dashed lines.

#### 4. Discussion

In this section, the striking effect of shear-thinning mediation (attenuation and even suppression) of elastic flow patterns and EIT is discussed. First, the critical conditions for the onset of EIT in shear-thinning fluids are reported. Data from the present work and experiments from the literature are then compiled to derive an empirical criterion for EIT suppression in strongly shear-thinning fluids, and possible mechanisms for such behaviour are discussed.

##### 4.1. Effect of shear-thinning on the transition to EIT

The transition to EIT, for some polymer solutions, is detected from the flow maps of ramp up experiments. Values of all parameters at the critical point are denoted using the superscript  $EIT$  and subscript  $c$ . Note that while some parameters are constant throughout the ramp up in Boger fluids (El, viscosity ratios etc.) their value depends on the shear-rate-variable viscosity in shear-thinning fluids.

In figure 17 a, the critical value  $Re_c^{EIT}$  is plotted as a function of  $1 - \bar{n}_e$  with colours representing the magnitude of  $\bar{El}$ . At first, increasing the shear-thinning behaviour leads to a decrease in the critical  $Re$  for the onset of EIT, with a simultaneous increase of elasticity. Above a critical shear-thinning index of 0.82 is reached ( $1 - \bar{n}_e = 0.18$ ), shear-thinning appears to delay the onset of EIT, despite the simultaneous significant increase in  $\bar{El}$  (figure 17 a).

A related non-monotonic trend can also be observed in figure 17 b) where  $Re_c^{EIT}$  is this time plotted against  $\bar{El}$ , with colour representing  $1 - \bar{n}_e$  values. For  $\bar{El} < 1$ , increasing  $\bar{El}$  together with a moderate decrease in the shear-thinning index ( $\bar{n}_e$  varying from 1 down to 0.82) leads to a decrease in  $Re_c^{EIT}$ . Further increase of  $\bar{El}$  above unity, together with a significant increase of the shear-thinning property, is associated with a delay of EIT.

The elasticity *versus* shear-thinning parameter space thus seems to indicate the existence of a critical point at  $\bar{n}_e = 0.82$  and  $El \sim 1$ . For  $0.82 > \bar{n}_e > 1$ , shear-thinning is

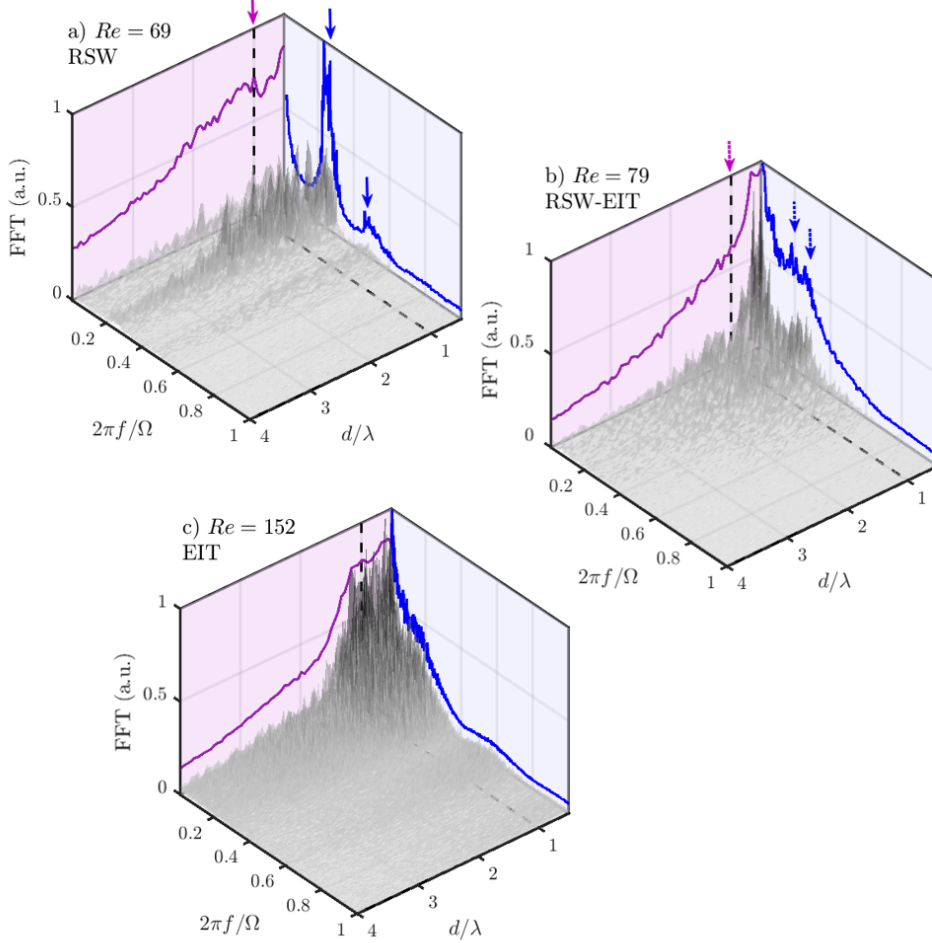


Figure 16: 2D FFT (time and space) of steady state experiments for the highly elastic, highly shear-thinning fluid (XG2000-50-2 experiment,  $\overline{El}=74$ ,  $\overline{n}_e=0.56$ ) at  $Re = 69$  (a),  $Re = 79$  (b) and  $Re = 152$  (c) corresponding respectively to RSW, RSW transitioning to EIT, and EIT. Spectra are plotted in arbitrary units along a temporal frequency axis scaled by the inner cylinder rotation frequency  $\Omega/2\pi$ , and a spatial wavelength axis where the wavelength is scaled by the gap width  $d$ . Space-averaged and time averaged 1D spectra are plotted in time-magnitude (blue) and space-magnitude (purple) planes respectively. Vertical arrows are guide to the eye showing peaks in both dimensions.

622 not sufficiently strong to disrupt the elastic destabilisation of the flow and the triggering  
 623 of EIT. However for  $\overline{n}_e < 0.82$ , even a large increase in elasticity is not sufficient to  
 624 promote the onset of EIT, which is delayed by shear-thinning. In other words, for fluids  
 625 with sufficiently strong shear-thinning rheology, the elastic instabilities are delayed by  
 626 the shear-thinning behaviour. This trend can be seen by plotting the critical values of  
 627  $El$  at the onset of EIT as a function of the critical values of  $1-n_e$  at this same onset in  
 628 figure 17 c). It is found that while  $El < 1$  is sufficient to trigger elastic instabilities for  
 629  $0.82 > n_e > 1$  (region R1 in sub-figure c), much higher values of  $El$  (several orders of  
 630 magnitude) are required for the onset of EIT if  $n_e < 0.82$  (region R2).



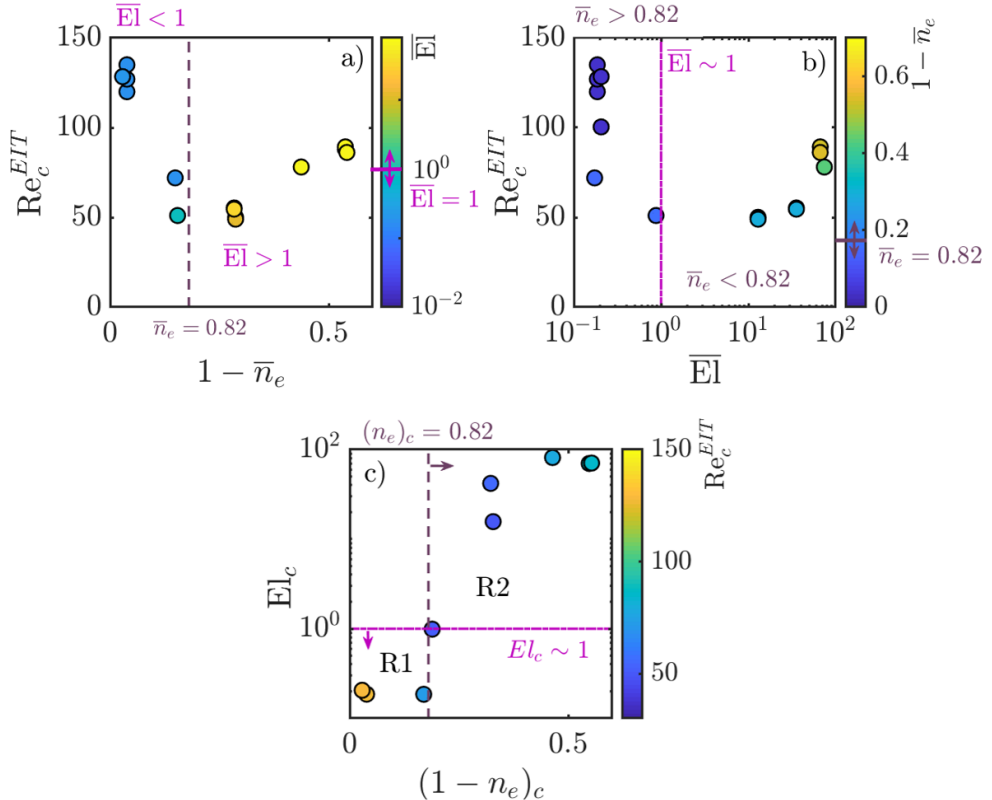


Figure 17: Critical Reynolds number value for the onset of EIT  $Re_c^{EIT}$  as a function of the averaged shear-thinning index (a) and elastic number (b). Marker colours on a and b indicate the values of  $\bar{El}$  and  $1 - \bar{n}_e$ , respectively. Vertical lines are plotted at  $n_e = 0.82$  and  $\bar{El} = 1$  on a and b respectively, and those threshold values are also reported on the colour-map of the conjugate figure (b and a respectively) as horizontal tick marks with arrows. Finally, sub-figure c) reports the critical values of  $El$  at the onset of EIT,  $El_c$ , as a function of the critical shear-thinning  $1 - n_e$  also at the onset.  $\bar{El} = 1$  and  $\bar{n}_e = 0.82$  thresholds are noted as horizontal and vertical dashed lines, respectively.

631

#### 4.2. Suppression of EIT

632

Although EIT is found to be delayed due to shear-thinning (eg. figure 13) in some experiments, it is not evidenced for  $Re < 300$  in many other experiments reported here. Newtonian-like transition patterns (figure 8), or RSW transitioning to WTVF (figure 10) have been observed instead. In figure 18, data from the present study (circles for XG, square for PAAM) are plotted together with experiments from the literature in a shear-thinning *versus* elasticity parameter space  $(1 - \bar{n}_e, \bar{El})$ . Experiments for which EIT has been reported in the Reynolds range measured (indicated in table 4) are denoted using white markers, while those for which EIT has not been observed (including the XG200-50 case with occasional RSW state, see figure 10) using black symbols. The flow transition patterns observed in these studies are also reported in table 4.

637

It should be noted that the data from the literature are not always fully characterised. For example in Groisman & Steinberg (1997), it is mentioned that the “apparent solution

642

643

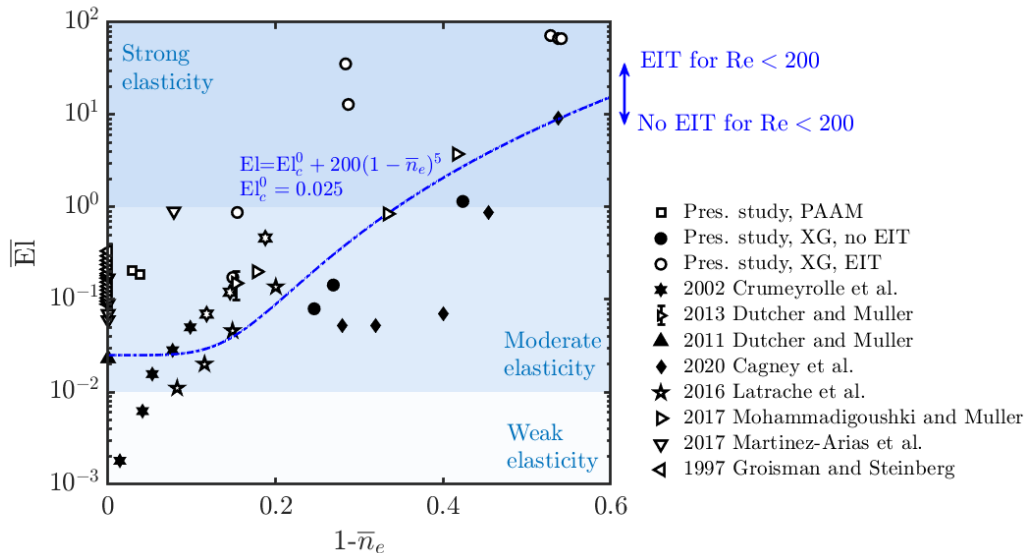


Figure 18: Shear-thinning *versus* elasticity parameter map in Taylor-Couette flows of polymeric solutions. Present study and literature experiments in the  $(1-\bar{n}_e, \bar{El})$  parameter space. White symbols indicate reported EIT, and black ones absence of it, for  $Re < Re_{max}$  as reported in table 4. The flow transition patterns observed in these studies are also reported in table 4.

644 viscosity was decreasing with increasing shear rate”, but the degree of shear-thinning was  
 645 not quantified. However their solvent viscosity was sufficiently high for the fluid to exhibit  
 646 mild shear-thinning at most, and their results are well within the moderate El range. A  
 647 study involving wormlike micellar solutions (WMS) is also reported (Mohammadigoushki  
 648 & Muller 2017), for which we estimate the shear-thinning index from the steady shear  
 649 rheological characterisation reported by the authors (figure 1).

650 The  $(1 - \bar{n}_e = 0, \bar{El})$  axis of figure 18 shows the existence of a critical value for  
 651  $\bar{El}$  beyond which EIT emerges for non-shear-thinning fluids. Below this curve, the  
 652 transitions are Newtonian-like due to the weak elasticity. This threshold value increases  
 653 with increased shear-thinning (increasing  $1 - \bar{n}_e$ ), so that for highly shear-thinning fluids,  
 654 no EIT may be observed, even in the high elasticity domain (figure 8). It may be  
 655 attributed to the fact that EIT is completely suppressed by shear-thinning, or that it  
 656 is simply delayed to  $Re_c$  values beyond the range studied. From comparison with the  
 657 literature (figure 18, table 4), it appears that this phenomenon is common to a variety  
 658 of polymers (including PEO (Crumeyrolle *et al.* 2002; Latrache *et al.* 2016), PAAM  
 659 (Groisman & Steinberg 1996) and XG (Cagney *et al.* 2020), present study) and even to  
 660 some extent to WMS (e.g. Mohammadigoushki & Muller (2017)). It becomes apparent  
 661 that EIT needs both high El and significant Re to develop, but that shear-thinning may  
 662 act to delay or even suppress elastic instabilities leading to EIT.

663 This can be expressed by an empirical criterion of the form

$$\bar{El} > El_c^0 + K \times (1 - \bar{n}_e)^\kappa, \quad (4.1)$$

664 where  $El_c^0 = 0.025$ ,  $K = 200$  and  $\kappa = 5$  are empirical parameters determined by visual  
 665 and iterative adjustment of equation 4.1 so that it separates empty from full markers

| Reference                           | Additive    | $AR$ | $\eta$ | $\frac{\mu_p}{\mu}$ | $\bar{n}_e$   | El               | $Re_{max}$ | Pattern                                      |
|-------------------------------------|-------------|------|--------|---------------------|---------------|------------------|------------|--|
| Present study                       | XG,<br>PAAM | 21.6 | 0.770  | 0.37-<br>1.0        | 0.46-<br>1.0  | 0.14-<br>74      | 300        | Various                                      |
| Cagney <i>et al.</i><br>(2020)      | XG          | 21.6 | 0.770  | 0.13-<br>1.0        | 0.46-<br>0.90 | 0.053-<br>9.03   | 1000       | CF-<br>TVF-<br>WTVF                          |
| Groisman & Stein-<br>berg (1996)    | PAAM        | 54.0 | 0.708  | 0.0083-<br>0.25     | N.A.          | 0.09-<br>0.34    | N.A.       | CF-<br>(TVF)-<br>(RSW)-<br>EIT               |
| Crumeyrole <i>et al.</i><br>(2002)  | PEO         | 46.6 | 0.883  | 0.16-<br>0.92       | 0.90-<br>0.98 | 0.0018-<br>0.050 | 200        | CF-<br>TVF-<br>WTVF<br>or CF-<br>TVF-<br>RIB |
| Dutcher & Muller<br>(2011)          | PEO         | 60.7 | 0.912  | 0.44                | 1.00          | 0-<br>0.023      | 200-250    | CF-<br>TVF-<br>WTVF                          |
| Dutcher & Muller<br>(2013)          | PEO         | 60.7 | 0.912  | 0.84                | 0.85          | 0.1-<br>0.2      | 200-250    | CF-<br>TVF-<br>RSW-<br>EIT                   |
| Latrache <i>et al.</i><br>(2016)    | PEO         | 46.6 | 0.883  | 0.83-<br>0.96       | 0.80-<br>0.92 | 0.011-<br>0.14   | 150        | CF-<br>TVF-<br>RIB-<br>EIT                   |
| Martínez-Arias &<br>Peixinho (2017) | PEO         | 30.0 | 0.909  | 0.083-<br>0.63      | 0.92-<br>1.00 | 0.06-<br>1.09    | 200        | CF-<br>TVF-<br>RSW-<br>EIT                   |
| Mohammadigoushki<br>& Muller (2017) | WMS         | 60.7 | 0.91   | $\sim$ 1.00         | 0.58-<br>0.82 | 0.2-<br>3.8      | 100        | CF-<br>(TVF/SVF)-<br>EIT                     |

Table 4: Flow transition patterns in shear-thinning and viscoelastic polymer or micellar solutions. N.A denotes quantities non-available or non-assessable from the available data.

in figure 18. The first one corresponds to the El threshold for Boger fluids, while the second and third ones describe the dependency of the El threshold on the shear-thinning index. Discrepancies in the data, especially for moderate shear-thinning ( $1 - \bar{n}_e \sim 0.1$ ) and elasticity may be attributed to the different geometrical parameters of the study reported (aspect ratio and radius ratio). It is indeed known that the streamline curvature has a great impact on the onset of purely elastic instabilities (Pakdel & McKinley 1996; Schaefer *et al.* 2018), and could similarly affect elasto-inertial instabilities. The empirical constants are thus likely to be related primarily to those geometrical parameters, and physical parameter of the fluid (temperature, molecular weight, shear-thinning viscosity, viscosity ratio etc) embedded into the  $\bar{\text{El}}$  and  $\bar{n}_e$  estimators. On the other hand, figure 18, table 4 and equation 4.1 show that data collected from experimental setup with various geometrical parameters and using various polymer or micellar solutions all follow this empirical behaviour. This could possibly suggest, if not a universal behaviour, at least a weak influence of some of the geometrical parameters in the shear-thinning mediation process.

#### 4.3. What are the mechanisms of shear-thinning mediation ?

The mechanisms for mediation of elasto-inertial features by shear-thinning remain to be explained. Intuitively, one may first postulate that for strong shear-thinning, radial viscosity gradients exist within the gap due to the strong base azimuthal flow, leading to a low viscosity inner core, and a high viscosity outer region. Viscous dissipation would then happen over a narrow range and an effective gap,  $d^r < d$ , would exist, with  $r_o^r < r_o$ ,  $r_o^r$  being the outer radius of the flowing region. This is comparable to the flow of shear-banding solutions (Perge *et al.* 2014).

The implications of this can be explored using simple scaling relations. Primarily, in the reduced gap, the apparent shear-rate for a given rotation speed increases:  $\dot{\gamma}^r = \Omega r_i / d^r > \dot{\gamma}$ . As a direct consequence, the Weissenberg number is increased:

$$\text{Wi}^r = \dot{\gamma}^r t_e > \text{Wi} \quad (4.2)$$

The apparent viscosity in the inner core (subject to higher shear rates  $\dot{\gamma}^r > \dot{\gamma}$ ) is expected to be lower than the apparent global viscosity in the full gap. Consequently, both the numerator and the denominator in the Re definition are reduced as a result of the gap reduction (equation 1.1). Simplifying the viscosity shear-rate dependency to a power law behaviour (introduced in section 1), one gets  $\mu^r \sim (\dot{\gamma}^r)^{n-1}$ , with typically  $-0.6 < n-1 < 1$ . Since  $\dot{\gamma}^r \sim 1/d^r$ , it follows that  $\mu^r \sim (d^r)^{1-n}$ , and

$$\text{Re}^r \sim \frac{\gamma^r (d^r)^2}{\mu^r} \sim \frac{(d^r)^{-1} (d^r)^2}{((d^r)^{-1})^{n-1}} \sim (d^r)^n, \quad (4.3)$$

and finally,

$$\text{El} \sim (d^r)^{-n-1}. \quad (4.4)$$

Since  $0 < n < 1$ , shear-thinning will cause a decrease in  $d^r$  which corresponds to a weak non-linear decrease in Re, but more importantly an increase in El. Thus, shear-thinning is not likely to be the case of reduced elastic instability, since it is conversely expected to promote elastic properties (i.e. increase Wi, El).

While this analysis has been based on a purely azimuthal CF, the radial viscosity gradient due to the main shear in the gap persists even for higher order flows. For example in Cagney & Balabani (2019b); Topayev *et al.* (2019), it is shown that Taylor vortices are squeezed and deform against the inner cylinder, in the lower viscosity inner region (Topayev *et al.* 2019). The previous scaling arguments on enhanced elasticity parameters

708 are thus likely to hold in more complex flows as well due to the base mean shear. On the  
 709 other hand, secondary flows such as Taylor vortices are also affected by shear-thinning  
 710 (Cagney & Balabani 2019b; Topayev *et al.* 2019), which in turn leads to axial viscosity  
 711 gradients. Such axial viscosity gradients could well be involved in the damping effect  
 712 of shear-thinning on transverse elastic waves. Results from section 3.5 also suggest that  
 713 shear-thinning damping of elastic waves must involve an interplay between inertia and  
 714 shear-thinning.

715 The effects of shear-thinning could thus be interpreted through a concept of preferential  
 716 flow paths, outside of which elastic waves may not be able to travel. Axial elastic  
 717 perturbations would thus be confronted with axial viscosity gradients which may act  
 718 as dampers. Moreover, the strength of the extensional deformations induced by such  
 719 perturbations would be reduced compared to the dominant radial shear rate, which is  
 720 also in turn enhanced by the radial viscosity distribution. An analogy to this mechanism  
 721 can be found in the recent work by Walkama *et al.* (2020), who performed an experimental  
 722 study of the onset of elastic instabilities (at vanishing  $Re$ ) in a microfluidic flow of PEO-  
 723 based Boger fluids past an array of cylinders. Spatial disorder was found to delay or  
 724 even suppress the onset of elastic instability. This was explained by the establishment, of  
 725 preferential flow paths governed by the geometry, where shear deformation of the polymer  
 726 is promoted over extensional deformation, having thus a stabilizing effects on the polymer  
 727 chains. Interestingly their results were also compared with a similar experiment using a  
 728 shear-thinning 3000 ppm xanthan gum solution (which may have featured significant  
 729 elasticity, however not quantified). No elastic instabilities were observed on a similar  
 730 range of  $Wi$  values despite the zero spatial disorder imposed, suggesting that shear-  
 731 thinning may act to suppress elastic disorder with mechanisms comparable to those of  
 732 spatial disorder.

## 733 5. Summary and conclusions

734 In this work, Taylor-Couette flow of polymer solutions of various degrees of elasticity  
 735 and shear-thinning were studied using flow-visualisation. Combined shear-thinning and  
 736 elasticity were found to globally de-stabilize the azimuthal Couette flow and favour  
 737 the onset of unsteady flow states with increased complexity (WTVF, SVF), sometimes  
 738 transitioning to chaotic and seemingly turbulent (RSW, EIT) even at relatively low  $Re$ .

739 Shear-thinning mediates the transition patterns of moderately to highly elastic polymer  
 740 solutions. In the absence of shear-thinning (Boger fluids), the flow transitioned to EIT  
 741 even at moderate elasticity levels. In contrast, in highly shear-thinning cases, moderate  
 742 to even high elasticity fluids may undergo Newtonian-like transition patterns, for which  
 743 no elasto-inertial instabilities occurred. Features of the flow states, such as the TVF  
 744 wavelength or the wavy frequency were also modified by the fluid's rheology. When both  
 745 shear-thinning and elasticity were moderate, elasto-inertial flow states (RSW, EIT) were  
 746 reported in some cases. It was found that their nature was modified by shear-thinning.  
 747 An increase in inertia tended to suppress chaos in the flow. Finally, in the most highly  
 748 elastic fluids that also had significant shear-thinning, the flow ultimately did transition  
 749 to EIT in a complex fashion. The Merge-Split Transition (MST) mechanism reported  
 750 in Lacassagne *et al.* (2020) for Boger fluids was also observed. However, the transition  
 751 occurred at elastic number values much higher than those required in the absence of  
 752 shear-thinning.

753 The global effect of shear-thinning was, thus, to delay or even suppress elasto-inertial  
 754 flow states, delaying their onset, occasionally damping chaotic features of the flow  
 755 when inertia was increased, or even completely suppressing EIT. For this last effect,

756 an empirical criterion for the existence of EIT was derived, also using results from the  
 757 literature on various polymer solutions. Experiments with additional polymers, WMS,  
 758 with a fully characterized rheology and in different geometrical configurations would be of  
 759 great interest to verify the universality of this criterion. The physical origin of the shear-  
 760 thinning mediation of elastic instabilities remains to be explained. It is not predicted by  
 761 scaling arguments but could be the consequence of axial viscosity gradients caused by  
 762 shear-thinning and secondary flows.

763 From a physical standpoint, both shear-thinning and viscoelastic properties originate  
 764 from the same fluid component: polymer chains. Disentangling the two effects is extremely  
 765 relevant from an empirical and applied point of view. It has, for example, recently been  
 766 applied in order to explain flow phenomena in micro-fluidic devices (Casanelas *et al.*  
 767 2016; Haward *et al.* 2020). Casanelas *et al.* (2016) showed that in the absence of inertia,  
 768 the Pakdel-McKinley criterion commonly used to describe the onset of purely elastic  
 769 instabilities does not systematically capture the effects of shear-thinning. By properly  
 770 characterising the fluid rheology, it may be possible to predict the existence, absence, or  
 771 damping of elasto-inertial regimes in a Taylor-Couette flow without further knowledge  
 772 or modelling of the state of polymer chains themselves. It is also evident that CF, TVF,  
 773 WTVF or EIT may be associated with different degrees of mixing performances, related  
 774 to flow unsteadiness and chaotic behaviour. Knowledge of very simple rheological fluid  
 775 parameters could thus allow to foresee, for a given amount of inertia, the performance  
 776 of a Taylor-Couette mixer in a shear-thinning and viscoelastic fluid. Tuning of such  
 777 rheological parameters by controlling either the solvent viscosity or the polymer nature  
 778 may in turn allow the mixing performances to be controlled and optimised.

## 779 Acknowledgements

780 Financial support for this work from the Engineering and Physical Sciences Research  
 781 Council (EPSRC) Manufacturing the Future programme (No.EP/N024915/1) is grate-  
 782 fully acknowledged.

## 783 Declaration of interests

784 The authors report no conflict of interest.

## REFERENCES

- 785 ABCHA, N., KELAI, F., LATRACHE, N., CRUMEYROLLE, O. & MUTABAZI, I. 2018 Radial  
 786 Propagation of the Instability Modes Observed in a Viscoelastic Couette–Taylor Flow.  
 787 In *Nonlinear Waves and Pattern Dynamics* (ed. N. Abcha, E. Pelinovsky & I. Mutabazi),  
 788 pp. 181–196. Cham: Springer International Publishing.
- 789 AKONUR, A. & LUEPTOW, R. M. 2003 Three-dimensional velocity field for wavy Taylor–Couette  
 790 flow. *Physics of Fluids* **15** (4), 947–960.
- 791 ALIBENYAHIA, B., LEMAITRE, C., NOUAR, C. & AIT-MESSAOUDENE, N. 2012 Revisiting the  
 792 stability of circular Couette flow of shear-thinning fluids. *Journal of Non-Newtonian Fluid*  
 793 *Mechanics* **183–184**, 37–51.
- 794 ANDERECK, C.D., LIU, S.S. & SWINNEY, H.L. 1986 Flow regimes in a circular Couette system  
 795 with independently rotating cylinders. *Journal of Fluid Mechanics* **164**, 155–183.
- 796 ASHRAFI, N. & KHAYAT, R. E. 2000 Shear-thinning-induced chaos in Taylor-Couette flow.  
 797 *Physical Review E* **61** (2), 1455–1467.
- 798 AVGOUSTI, M. & BERIS, A. N. 1993 Non-axisymmetric modes in viscoelastic taylor-couette  
 799 flow. *Journal of Non-Newtonian Fluid Mechanics* **50** (2), 225–251.

- 800 BAHRANI, S. A., NOUAR, C., NEVEU, A. & BECKER, S. 2015 Transition to chaotic Taylor-  
801 Couette flow in shear-thinning fluids. p. 11. Lyon.
- 802 BARLOW, H. J., HEMINGWAY, E. J., CLARKE, A. & FIELDING, S. M. 2019 Linear instability of  
803 shear thinning pressure driven channel flow. *Journal of Non-Newtonian Fluid Mechanics*  
804 **270**, 66–78.
- 805 BAUMERT, B. M. & MULLER, S. J. 1997 Flow regimes in model viscoelastic fluids in a circular  
806 couette system with independently rotating cylinders. *Physics of Fluids* **9** (3), 566–586.
- 807 BAUMERT, B. M. & MULLER, S. J. 1999 Axisymmetric and non-axisymmetric elastic and  
808 inertio-elastic instabilities in Taylor–Couette flow. *Journal of Non-Newtonian Fluid*  
809 *Mechanics* **83** (1), 33–69.
- 810 BODIGUEL, H., BEAUMONT, J., MACHADO, A., MARTINIE, L., KELLAY, H. & COLIN, A. 2015  
811 Flow Enhancement due to Elastic Turbulence in Channel Flows of Shear Thinning Fluids.  
812 *Physical Review Letters* **114** (2), 028302.
- 813 BOGER, D. V. 1977 A highly elastic constant-viscosity fluid. *Journal of Non-Newtonian Fluid*  
814 *Mechanics* (3), 87–89.
- 815 CAGNEY, N. & BALABANI, S. 2019a Influence of Shear-Thinning Rheology on the Mixing  
816 Dynamics in Taylor-Couette Flow. *Chemical Engineering & Technology* **42** (8), 1680–  
817 1690.
- 818 CAGNEY, N. & BALABANI, S. 2019b Taylor-Couette flow of shear-thinning fluids. *Physics of*  
819 *Fluids* **31** (5), 053102.
- 820 CAGNEY, NEIL, LACASSAGNE, TOM & BALABANI, STAVROULA 2020 Taylor–Couette flow  
821 of polymer solutions with shear-thinning and viscoelastic rheology. *Journal of Fluid*  
822 *Mechanics* **905**.
- 823 CASANELLAS, L., ALVES, M. A., POOLE, R. J., LEROUGE, S. & LINDNER, A. 2016 The  
824 stabilizing effect of shear thinning on the onset of purely elastic instabilities in serpentine  
825 microflows. *Soft Matter* **12** (29), 6167–6175.
- 826 CATON, F. 2006 Linear stability of circular Couette flow of inelastic viscoplastic fluids. *Journal*  
827 *of Non-Newtonian Fluid Mechanics* **134** (1), 148–154.
- 828 CHHABRA, R. P. & RICHARDSON, J. F. 1999 *Non-Newtonian Flow in the Process Industries:*  
829 *Fundamentals and Engineering Applications*. Butterworth-Heinemann.
- 830 COLE, J. A. 1976 Taylor-vortex instability and annulus-length effects. *Journal of Fluid*  
831 *Mechanics* **75** (1), 1–15.
- 832 COLES, DONALD 1965 Transition in circular Couette flow. *Journal of Fluid Mechanics* **21** (3),  
833 385–425.
- 834 CORONADO-MATUTTI, O., SOUZA MENDES, P. R. & CARVALHO, M. S. 2004 Instability  
835 of Inelastic Shear-Thinning Liquids in a Couette Flow Between Concentric Cylinders.  
836 *Journal of Fluids Engineering* **126** (3), 385–390.
- 837 COUGHLIN, K. T. & MARCUS, P. S. 1992a Modulated waves in Taylor-Couette flow Part 1.  
838 Analysis. *Journal of Fluid Mechanics* **234**, 1–18.
- 839 COUGHLIN, K. T. & MARCUS, P. S. 1992b Modulated waves in Taylor-Couette flow Part 2.  
840 Numerical simulation. *Journal of Fluid Mechanics* **234**, 19–46.
- 841 CRUMEYROLLE, O, LATRACHE, N, MUTABAZI, I & EZERSKY, A B 2005 Instabilities with shear-  
842 thinning polymer solutions in the Couette-Taylor system. *Journal of Physics: Conference*  
843 *Series* **14**, 78–93.
- 844 CRUMEYROLLE, O., MUTABAZI, I. & GRISEL, M. 2002 Experimental study of inertioelastic  
845 Couette–Taylor instability modes in dilute and semidilute polymer solutions. *Physics of*  
846 *Fluids* **14** (5), 1681–1688.
- 847 DIVOUX, T., FARDIN, M. A., MANNEVILLE, S. & LEROUGE, S. 2016 Shear Banding of Complex  
848 Fluids. *Annual Review of Fluid Mechanics* **48** (1), 81–103.
- 849 DUTCHER, C. S. & MULLER, S. J. 2009 Spatio-temporal mode dynamics and higher order  
850 transitions in high aspect ratio Newtonian Taylor–Couette flows. *Journal of Fluid*  
851 *Mechanics* **641**, 85–113.
- 852 DUTCHER, C. S. & MULLER, S. J. 2011 Effects of weak elasticity on the stability of high  
853 Reynolds number co- and counter-rotating Taylor-Couette flows. *Journal of Rheology*  
854 **55** (6), 1271–1295.
- 855 DUTCHER, C. S. & MULLER, S. J. 2013 Effects of moderate elasticity on the stability of co-  
856 and counter-rotating Taylor–Couette flows. *Journal of Rheology* **57** (3), 791–812.

- 857 ELÇIÇEK, H. & GÜZEL, B. 2020a Effect of shear-thinning behavior on flow regimes in  
858 Taylor–Couette flows. *Journal of Non-Newtonian Fluid Mechanics* **279**, 104277.
- 859 ELÇIÇEK, H. & GÜZEL, B. 2020b On non-axisymmetric flow structures of graphene  
860 suspensions in Taylor–Couette reactors. *International Journal of Environmental Science  
861 and Technology* .
- 862 ESCUDIER, M. P., GOULDSON, I. W. & JONES, D. M. 1995 Taylor vortices in Newtonian and  
863 shear-thinning liquids. *Proceedings of the Royal Society of London. Series A: Mathematical  
864 and Physical Sciences* **449** (1935), 155–176.
- 865 FARDIN, M. A., J. OBER, T., GRENARD, V., DIVOUX, T., MANNEVILLE, S., H. MCKINLEY,  
866 G. & LEROUGE, S. 2012 Interplay between elastic instabilities and shear-banding: three  
867 categories of Taylor–Couette flows and beyond. *Soft Matter* **8** (39), 10072–10089.
- 868 FARDIN, M. A., LOPEZ, D., CROSO, J., GRÉGOIRE, G., CARDOSO, O., MCKINLEY, G. H.  
869 & LEROUGE, S. 2010 Elastic Turbulence in Shear Banding Wormlike Micelles. *Physical  
870 Review Letters* **104** (17), 178303.
- 871 FARDIN, M. A., PERGE, C. & TABERLET, N. 2014 “The hydrogen atom of fluid dynamics” –  
872 introduction to the Taylor–Couette flow for soft matter scientists. *Soft Matter* **10** (20),  
873 3523–3535.
- 874 FENSTERMACHER, P. R., SWINNEY, HARRY L. & GOLLUB, J. P. 1979 Dynamical instabilities  
875 and the transition to chaotic Taylor vortex flow. *Journal of Fluid Mechanics* **94** (1),  
876 103–128.
- 877 GILLISSEN, J. J. J. 2019 Two-dimensionnal decaying elastoinertial turbulence. *Physical Review  
878 Letters* **123** (14), 144502.
- 879 GROISMAN, A. & STEINBERG, V. 1996 Couette-Taylor Flow in a Dilute Polymer Solution.  
880 *Physical Review Letters* **77** (8), 1480–1483.
- 881 GROISMAN, A. & STEINBERG, V. 1997 Solitary Vortex Pairs in Viscoelastic Couette Flow.  
882 *Physical Review Letters* **78** (8), 1460–1463.
- 883 GROISMAN, A. & STEINBERG, V. 2000 Elastic turbulence in a polymer solution flow. *Nature*  
884 **405** (6782), 53.
- 885 GROISMAN, A. & STEINBERG, V. 2004 Elastic turbulence in curvilinear flows of polymer  
886 solutions. *New Journal of Physics* **6**, 29–29.
- 887 GROSSMANN, S., LOHSE, D. & SUN, C. 2016 High–Reynolds Number Taylor-Couette  
888 Turbulence. *Annual Review of Fluid Mechanics* **48** (1), 53–80.
- 889 GUL, M., ELSINGA, G. E. & WESTERWHEEL, J. 2018 Experimental investigation of torque  
890 hysteresis behaviour of Taylor–Couette Flow. *Journal of Fluid Mechanics* **836**, 635–648.
- 891 HAWARD, S. J., HOPKINS, C. C. & SHEN, A. Q. 2020 Asymmetric flow of polymer solutions  
892 around microfluidic cylinders: Interaction between shear-thinning and viscoelasticity.  
893 *Journal of Non-Newtonian Fluid Mechanics* p. 104250.
- 894 HOPKINS, CAMERON C., HAWARD, SIMON J. & SHEN, AMY Q. 2020 Purely Elastic  
895 Fluid–Structure Interactions in Microfluidics: Implications for Mucociliary Flows. *Small*  
896 **16** (9), 1903872.
- 897 JAMES, D. F. 2009 Boger Fluids. *Annual Review of Fluid Mechanics* **41** (1), 129–142.
- 898 LACASSAGNE, T., CAGNEY, N., GILLISSEN, J. J. J. & BALABANI, S. 2020 Vortex merging  
899 and splitting: A route to elastoinertial turbulence in Taylor-Couette flow. *Physical Review  
900 Fluids* **5** (11), 113303.
- 901 LANGE, M. & ECKHARDT, B. 2001 Vortex pairs in viscoelastic Couette-Taylor flow. *Physical  
902 Review E* **64** (2), 027301.
- 903 LARSON, R. G. & DESAI, P. S. 2015 Modeling the Rheology of Polymer Melts and Solutions.  
904 *Annual Review of Fluid Mechanics* **47** (1), 47–65.
- 905 LARSON, R. G. 2000 Turbulence without inertia. *Nature* **405** (6782), 27–28.
- 906 LARSON, R. G., MULLER, S. J. & SHAQFEH, E. S. G. 1994 The effect of fluid rheology on  
907 the elastic Taylor-Couette instability. *Journal of Non-Newtonian Fluid Mechanics* **51** (2),  
908 195–225.
- 909 LARSON, R. G., SHAQFEH, E. S. G. & MULLER, S. J. 1990 A purely elastic instability in  
910 Taylor–Couette flow. *Journal of Fluid Mechanics* **218**, 573–600.
- 911 LATRACHE, N., ABCHA, N., CRUMEYROLLE, O. & MUTABAZI, I. 2016 Defect-mediated  
912 turbulence in ribbons of viscoelastic Taylor-Couette flow. *Physical Review E* **93** (4),  
913 043126.



- 914 LATRACHE, N., CRUMEYROLLE, O. & MUTABAZI, I. 2012 Transition to turbulence in a flow of  
915 a shear-thinning viscoelastic solution in a Taylor-Couette cell. *Physical Review E* **86** (5),  
916 056305.
- 917 LIU, N. & KHOMAMI, B. 2013 Elastically induced turbulence in Taylor–Couette flow: direct  
918 numerical simulation and mechanistic insight. *Journal of Fluid Mechanics* **737**, R4.
- 919 LOCKETT, T. J., RICHARDSON, S. M. & WORRAKER, W. J. 1992 The stability of inelastic  
920 non-Newtonian fluids in Couette flow between concentric cylinders: a finite-element study.  
921 *Journal of Non-Newtonian Fluid Mechanics* **43** (2), 165–177.
- 922 MARTÍNEZ-ARIAS, B. & PEIXINHO, J. 2017 Torque in Taylor–Couette flow of viscoelastic  
923 polymer solutions. *Journal of Non-Newtonian Fluid Mechanics* **247**, 221–228.
- 924 MASUDA, H., HORIE, T., HUBACZ, R., OHTA, M. & OHMURA, N. 2017 Prediction of onset of  
925 Taylor-Couette instability for shear-thinning fluids. *Rheologica Acta* **56** (2), 73–84.
- 926 MOHAMMADIGOUSHKI, H. & MULLER, S. J. 2017 Inertio-elastic instability in Taylor-Couette  
927 flow of a model wormlike micellar system. *Journal of Rheology* **61** (4), 683.
- 928 PAKDEL, P. & MCKINLEY, G. H. 1996 Elastic Instability and Curved Streamlines. *Physical*  
929 *Review Letters* **77** (12), 2459–2462.
- 930 PERGE, C., FARDIN, M. A. & MANNEVILLE, S. 2014 Inertio-elastic instability of non shear-  
931 banding wormlike micelles. *Soft Matter* **10** (10), 1450–1454.
- 932 RAMESH, P. & ALAM, M. 2020 Interpenetrating spiral vortices and other coexisting states in  
933 suspension Taylor-Couette flow. *Physical Review Fluids* **5** (4), 042301.
- 934 RAMESH, P., BHARADWAJ, S. & ALAM, M. 2019 Suspension Taylor–Couette flow: co-existence  
935 of stationary and travelling waves, and the characteristics of Taylor vortices and spirals.  
936 *Journal of Fluid Mechanics* **870**, 901–940.
- 937 SCHAEFER, C., MOROZOV, A. & WAGNER, C. 2018 Geometric scaling of elastic instabilities  
938 in the Taylor-Couette geometry: A theoretical, experimental and numerical study.  
939 *arXiv:1806.00328 [cond-mat, physics:physics]* .
- 940 SINEVIC, V., KUBOI, R. & NIENOW, A. W. 1986 Power numbers, Taylor numbers and Taylor  
941 vortices in viscous newtonian and non-newtonian fluids. *Chemical Engineering Science*  
942 **41** (11), 2915–2923.
- 943 STEINBERG, V. 2019 Scaling Relations in Elastic Turbulence. *Physical Review Letters* **123** (23),  
944 234501.
- 945 STEINBERG, V. & GROISMAN, A. 1998 Elastic versus inertial instability in Couette-Taylor flow  
946 of a polymer solution: Review. *Philosophical Magazine B* **78** (2), 253–263.
- 947 TAYLOR, G. I. 1923 Stability of a viscous liquid contained between two rotating cylinders.  
948 *Philosophical Transactions of the Royal Society of London. Series A, Containing Papers*  
949 *of a Mathematical or Physical Character* **223** (605-615), 289–343.
- 950 THOMAS, D. G., SURESHKUMAR, R. & KHOMAMI, B. 2006 Pattern Formation in Taylor-Couette  
951 Flow of Dilute Polymer Solutions: Dynamical Simulations and Mechanism. *Physical*  
952 *Review Letters* **97** (5), 054501.
- 953 TOPAYEV, S., NOUAR, C., BERNARDIN, D., NEVEU, A. & BAHRANI, S. A. 2019 Taylor-vortex  
954 flow in shear-thinning fluids. *Physical Review E* **100** (2), 023117.
- 955 VARSHNEY, A. & STEINBERG, V. 2019 Elastic Alfvén waves in elastic turbulence. *Nature*  
956 *Communications* **10** (1), 1–7.
- 957 VOLK, A. & KÄHLER, C. J. 2018 Density model for aqueous glycerol solutions. *Experiments in*  
958 *Fluids* **59** (5).
- 959 WALKAMA, D. M., WAISBORD, N. & GUASTO, J. S. 2020 Disorder Suppresses Chaos in  
960 Viscoelastic Flows. *Physical Review Letters* **124** (16), 164501.
- 961 WHITE, J. M. & MULLER, S. J. 2002a Experimental studies on the stability of Newtonian  
962 Taylor–Couette flow in the presence of viscous heating. *Journal of Fluid Mechanics* **462**,  
963 133–159.
- 964 WHITE, J. M. & MULLER, S. J. 2002b The role of thermal sensitivity of fluid properties,  
965 centrifugal destabilization, and nonlinear disturbances on the viscous heating instability  
966 in Newtonian Taylor–Couette flow. *Physics of Fluids* **14** (11), 3880–3890.
- 967 ZIRNSAK, M. A., BOGER, D. V. & TIRTAATMADJA, V. 1999 Steady shear and dynamic  
968 rheological properties of xanthan gum solutions in viscous solvents. *Journal of Rheology*  
969 **43** (3), 627–650.
- 970 ÖZTEKIN, A., BROWN, R. A. & MCKINLEY, G. H. 1994 Quantitative prediction of the

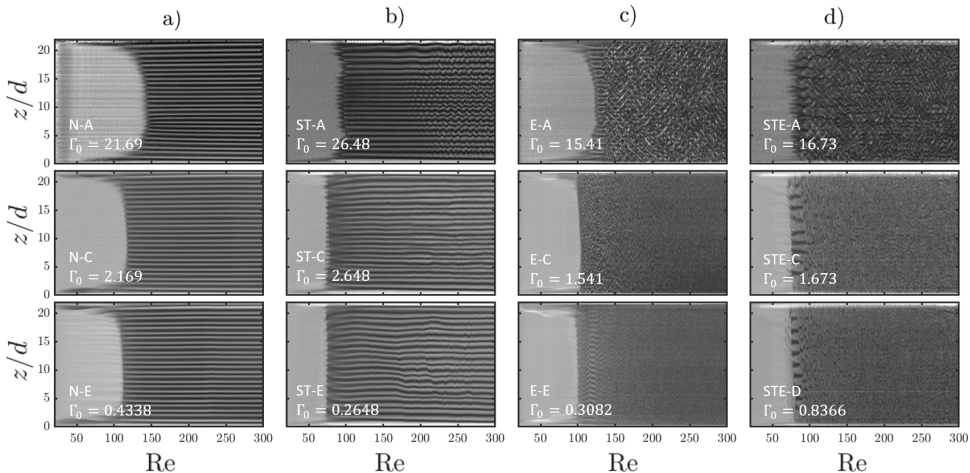


Figure 19: Flow maps of fastest (top row) to lowest (bottom row) ramp up experiments for a Newtonian fluid (N, first column, a), Shear-thinning fluid with a Newtonian-like transition (ST, second column, b), purely elastic Boger fluid (E, third column, c), and shear-thinning fluid with strong elasticity (STE, fourth column, d). The fluid type (N, ST, E, STE), run index (A to E) and maximum NDAR  $\Gamma_0$  are reported in each sub-figure.

971 viscoelastic instability in cone-and-plate flow of a Boger fluid using a multi-mode Giesekus  
 972 model. *Journal of Non-Newtonian Fluid Mechanics* **54**, 351–377.

### 973 Appendix A. Effect of non-dimensional acceleration rate

974 In this appendix, dedicated ramp up experiments are performed. For each fluid, several  
 975 tests are performed, in which  $Re_{max}$  is kept constant, and  $d\Omega/dt$  and experiment duration  
 976 are varied over several decades to induce variations of  $\Gamma_0$ .

977 Five fluids corresponding to four different typical behaviours are studied: a Newtonian  
 978 case (N72, noted N), a shear-thinning dominated case case, with a Newtonian-like  
 979 transition sequence (XG1000-25, noted ST), a purely elastic, Boger fluid (P500-72, noted  
 980 E), and a fluid with shear-thinning but dominant elasticity (XG2000-72, noted STE).  
 981 Experimental conditions for all tests are detailed in table 5.

982 The frequency map tool can not be used in the following analysis. Indeed, when varying  
 983  $d\Omega/dt$ , the recording frequency has to be adapted in order to achieve similar Re-resolution  
 984 flow maps regardless of the acceleration. In other words,  $f_s/f_{max}$  has to be kept constant  
 985 (typically above 3). Yet, the  $N_c$  segment must be long enough to capture low frequency  
 986 events, even at high frame rates. Capturing a similar wave frequency  $f_w$ , with the same  
 987  $f_s/f_{max}$  ratio, would require to increase  $N_c$  proportionally to  $f_s$  (in order of magnitude).  
 988 The sampling time and Re variations corresponding to  $N_c$  may then become too large to  
 989 assume that Re stays constant within the sampled sequence. Frequency maps can thus  
 990 not be used systematically to describe fast ramp up experiments, and we are here limited  
 991 to the qualitative study of flow states and to the quantification of transitions through  
 992 flow maps. This is however a physical process more due to the acceleration rate itself  
 993 rather than an experimental limitation: ramping up faster than a typical wave time-scale  
 994 does not allow a wave or perturbation with this time-scale to develop in a steady manner,  
 995 and thus to be captured in a frequency map.

| Sample    | Test | $f_s$<br>Hz | $1/\Delta Re$ | $\Omega_{max}$<br>$s^{-1}$ | $d\Omega/dt$<br>$s^{-2}$ | $\Gamma_0$ | Expected behaviour |
|-----------|------|-------------|---------------|----------------------------|--------------------------|------------|--------------------|
| N72       | A    | 3000        | 179           | 66.96                      | 3.732                    | 21.69      | N                  |
| N72       | B    | 1500        | 179           | 66.96                      | 1.866                    | 10.85      | N                  |
| N72       | C    | 300         | 179           | 66.96                      | 0.3732                   | 2.169      | N                  |
| N72       | D    | 150         | 179           | 66.96                      | 0.1866                   | 1.085      | N                  |
| N72       | E*   | 75          | 224           | 66.96                      | 0.07463                  | 0.4338     | N                  |
| N72       | F*   | 30          | 202           | 66.96                      | 0.03317                  | 0.1928     | N                  |
| XG1000-25 | A    | 3000        | 200           | 46.84                      | 2.229                    | 26.48      | ST                 |
| XG1000-25 | B    | 1500        | 200           | 46.84                      | 1.115                    | 13.24      | ST                 |
| XG1000-25 | C    | 300         | 200           | 46.84                      | 0.2229                   | 2.648      | ST                 |
| XG1000-25 | D    | 150         | 200           | 46.84                      | 0.1115                   | 1.324      | ST                 |
| XG1000-25 | E*   | 30          | 200           | 46.84                      | 0.02229                  | 0.2648     | ST                 |
| P500-72   | A    | 4000        | 226           | 99.23                      | 5.822                    | 15.41      | E                  |
| P500-72   | B    | 2000        | 226           | 99.23                      | 2.911                    | 7.706      | E                  |
| P500-72   | C    | 400         | 226           | 99.23                      | 0.5822                   | 1.541      | E                  |
| P500-72   | D*   | 200         | 226           | 99.23                      | 0.2911                   | 0.7706     | E                  |
| P500-72   | E*   | 90          | 253           | 99.23                      | 0.1164                   | 0.3082     | E                  |
| XG2000-50 | A    | 4000        | 230           | 82.75                      | 4.396                    | 16.73      | STE                |
| XG2000-50 | B    | 2000        | 230           | 82.75                      | 2.198                    | 8.366      | STE                |
| XG2000-50 | C    | 400         | 230           | 82.75                      | 0.4396                   | 1.673      | STE                |
| XG2000-50 | D*   | 200         | 230           | 82.75                      | 0.2198                   | 0.8366     | STE                |

Table 5: Experimental conditions: influence of ramp up acceleration rate. Experiments are conducted for samples expected to exhibit different behaviours: Newtonian (N) figure 6, Purely shear-thinning as described in figure 8 (ST) where elastic instabilities are suppressed by shear-thinning, purely elastic Boger fluid (E) (figure 7) with negligible shear-thinning, and shear-thinning dominated by elasticity (STE) figure 13. \* denotes experiments with  $\Gamma_0 < 1$  also reported in table 2.

996 In the Newtonian case (figure 19, left column, a), the flow maps are qualitatively  
997 similar for very different acceleration rates. However, the exact Reynolds number  $Re_c^{TVF}$   
998 for the CF to TVF transition increases for the largest  $\Gamma_0$  (a). Values of  $Re_c^{TVF}$  and  $\lambda$  are  
999 plotted against  $d\Omega/dt$  and  $\Gamma_0$  in figure 20, for all N runs in table 5 (along with the critical  
1000 Reynolds number for the onset of WTVF,  $Re_c^{WTVF}$ , for the two lowest acceleration cases  
1001 for which frequency maps can still be constructed). It appears that for  $\Gamma_0 < 1$ , the  
1002 onset of TVF is not affected by the value of the acceleration rate as expected from the  
1003 observations of Dutcher & Muller (2009).

1004 For the shear-thinning dominated case (figure 8), the flow maps are also not qualita-  
1005 tively affected. Note that in the fastest acceleration's case, one can clearly identify the  
1006 waviness of Taylor vortices just from the flow map (d). Figure 20 ST shows that for  
1007  $\Gamma_0 < 3$  the critical Reynolds number for CF to TVF transition does not depend on  $\Gamma_0$ .

1008 The results for the purely elastic case are qualitatively different in terms of flow states  
1009 transition. From figure 19 (third column, c), it appears that the RSW is modified by the  
1010 variations in acceleration rates. The Reynolds range in which it can be found reduces  
1011 with increasing  $\Gamma_0$ , as illustrated in figure 20 where critical Reynolds numbers are plotted  
1012 as a function of  $\Gamma_0$ . In the fastest acceleration case, it is difficult to tell whether the state  
1013 observed from  $Re = 100$  to about  $Re = 120$  is TVF or RSW (this would require the use of  
1014 frequency maps) but the flow signature is definitely different from low acceleration RSW.  
1015 As in the N and ST cases, the onset of TVF is also delayed for high  $\Gamma_0$  values, and  $Re_c^{TVF}$

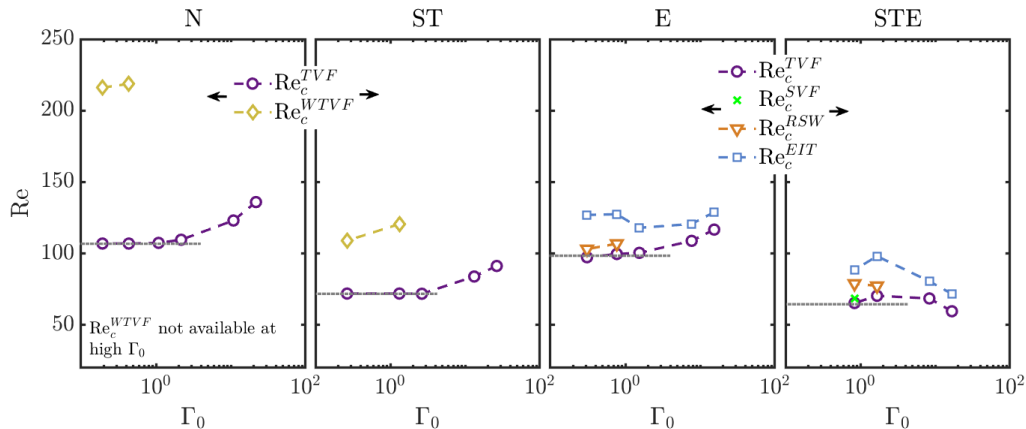


Figure 20: Values of critical Reynolds number for the onset of various flow states in the four investigated cases: Newtonian (N), shear-thinning with Newtonian-like transitions (ST), purely elastic Boger (E) and shear-thinning with elastic flow patterns (STE).

1016 can be assumed acceleration-independent for  $\Gamma_0 < 1$ . However values of  $Re_c^{EIT}$  are almost  
 1017 constant for all accelerations. This, in turn, leads to a narrowing of the Reynolds range  
 1018 left for the two intermediate regimes (TVF, RSW), i.e. regimes comprised between the  
 1019 base flow state (CF) and the ultimate elasto-inertial flow state (EIT). In other words,  
 1020 ramping up the inner cylinder at high acceleration rates leads to a “squeezing” of the  
 1021 intermediate transition steps in favour of an abrupt CF to EIT transition. Note that  
 1022 once again the “temporal” frequencies (patterns along Re axis) for RSW or EIT are  
 1023 more visible on the flow map in the fast cases, as the fast ramp up leads to capture only  
 1024 a limited number of waves period, but describe them with great resolution, even though  
 1025 that description spans a significant Re variation.

1026 For the final case of a fluid where strong shear-thinning is dominated by elasticity  
 1027 (STE) we consider the XG2000-50 case studied previously (figures 13,14,15,16). Note  
 1028 that the XG1000-72 case has also been investigated and leads to results similar to the  
 1029 E case. As in the E case, suppression of intermediate regimes (TVF, RSW, SVF) is  
 1030 reported. Contrary to the previous cases however, the onset of the TVF flow is not  
 1031 affected as  $Re_c^{TVF}$  does not show any clear trend with  $\Gamma_0$ . On the other hand, it is the  
 1032 earlier onset of EIT that leads to the “squeezing” of the intermediate Reynolds range.

1033 From a qualitative point of view and in terms of succession of flow states, the N and  
 1034 ST cases are acceleration-independent, but E and STE fluids may have intermediate  
 1035 regimes suppressed for  $\Gamma_0 \gg 1$ . From a quantitative point of view, the CF to TVF  
 1036 transition is in general not affected by the acceleration rate for rates lower than unity (but  
 1037 higher acceleration rates may even be used in the ST case). To extend this acceleration  
 1038 study, it would be suitable to adapt the frequency maps analysis to highest acceleration  
 1039 rates, and adapt the dimensional acceleration rates to achieve constant non-dimensional  
 1040 acceleration rates throughout the ramp up for shear-thinning fluids, as done in Dutcher  
 1041 & Muller (2013).